Bulletin of the Seismological Society of America, Vol. XX, No. XX, pp. –, – 2019, doi: 10.1785/0120180320

Ⓔ

Long-Period Ground Motions from Past and Virtual Megathrust Earthquakes along the Nankai Trough, Japan

by Loïc Viens* and Marine A. Denolle

Abstract Long-period ground motions from large ($M_w \geq 7.0$) subduction-zone earthquakes are a real threat for large-scale human-made structures. The Nankai subduction zone, Japan, is expected to host a major megathrust earthquake in the near future and has therefore been instrumented with offshore and onshore permanent seismic networks. We use the ambient seismic field continuously recorded at these stations to simulate the long-period (4–10 s) ground motions from past and future potential offshore earthquakes. First, we compute impulse response functions (IRFs) between an ocean-bottom seismometer of the Dense Oceanfloor Network System for Earthquakes and Tsunamis (DONET) network, which is located offshore on the accretionary wedge, and 60 onshore Hi-net stations using seismic interferometry by deconvolution. As this technique only preserves the relative amplitude information of the IRFs, we use a moderate M_w 5.5 event to calibrate the amplitudes to absolute levels. After calibration, the IRFs are used together with a uniform stress-drop source model to simulate the long-period ground motions of the 2004 M_w 7.2 intraplate earthquake. For both events, the residuals of the 5% damped spectral acceleration (SA) computed from the horizontal and vertical components of the observed and simulated waveforms exhibit almost no bias and acceptable uncertainties. We also compare the observed SA values of the M_w 7.2 event to those from the subduction-zone BC Hydro ground-motion model (GMM) and find that our simulations perform better than the model. Finally, we simulate the long-period ground motions of a hypothetical M_w 8.0 subduction earthquake that could occur along the Nankai trough. For this event, our simulations generally exhibit stronger long-period ground motions than those predicted by the BC Hydro GMM. This study suggests that the ambient seismic field recorded by the ever-increasing number of ocean-bottom seismometers can be used to simulate the long-period ground motions from large megathrust earthquakes.

Supplemental Content: Text and figures detailing the raw impulse response functions (IRFs) from the KMD14 virtual source, the correction applied to the IRF amplitudes to account for the nonuniform source of the ambient seismic field, and the raw IRFs and noise levels at the KMC10 and KMC11 virtual sources, the effect of the surface-wave radiation pattern at periods longer than 10 s for the two earthquakes, the determination of the source parameters for the simulation of the M_w 7.2 earthquake, and the attenuation of spectral acceleration values with distance for the M_w 7.2 event.

Introduction

Large ($M_w \geq 7.0$) subduction-zone earthquakes can generate strong and long-duration low-frequency seismic waves at great distances from the source. Such ground motions are generally the result of an efficient propagation of seismic waves through elastic structures such as accretionary wedges or sedimentary basins (Koketsu *et al.*, 2008). In urban environments, long-period seismic waves are of particular concern due to the increasing number of large-scale structures such as tall buildings and long-span bridges. One of the worst examples of damage caused by long-period ground motions occurred during the 1985 M_w 8.0 Michoacán earthquake in Mexico City, where hundreds of buildings were destroyed or badly damaged due to sedimentary basin amplification

*Now at Disaster Prevention Research Institute, Kyoto University, Gokasho, Uji, Kyoto 611-0011, Japan.

(Anderson *et al.*, 1986; Beck and Hall, 1986). Another example is the serious damage to large oil-storage tanks in the city of Tomakomai, Japan, caused by the long-period ground motions from the 2003 M_w 8.3 Tokachi-Oki earthquake, which occurred more than 250 km away offshore (Koketsu *et al.*, 2005).

To assess the seismic hazard related to short- and long-period ground motions, ground-motion models (GMMs), also called ground-motion prediction equations, have been developed specifically for subduction-zone earthquakes (e.g., Crouse *et al.*, 1988; Youngs *et al.*, 1997; Atkinson and Boore, 2003, 2008; Zhao *et al.*, 2006; BC Hydro, 2012; Abrahamson *et al.*, 2016). These empirical relations relate the source, path, and site parameters to the ground-motion levels from intraplate and interplate earthquakes in subduction zones and generally capture well the characteristics of the high-frequency ground motions, including nonlinear effects. For a specific subduction zone, however, the crustal structure (e.g., accretionary wedge and sedimentary basin effects) may have a strong influence on the long-period ground motions, which might not be adequately represented by GMMs. This is in part due to the fact that GMMs are generally developed using strong ground motion records from different regions and may not contain the path effect relevant to a specific subduction zone. To better understand the long-period wave propagation effects from offshore subduction events, physics-based simulations using simple but realistic velocity models of subduction zones have been performed (e.g., Furumura *et al.*, 2008; Yoshimura *et al.*, 2008; Guo *et al.*, 2016). These simulations indicate that accretionary wedges may attenuate long-period ground motions but extend their duration through the development of complex coda waves. Although these conclusions agree relatively well with observed earthquake waveforms, simulations are still limited by our imperfect knowledge of the elastic and anelastic structure of the Earth, especially near the trench.

In the last decade, seismic interferometry has become very popular in seismology. Under certain conditions, the cross correlation of ambient seismic field records at two seismometers is proportional to the elastodynamic response of the Earth, or impulse response function (IRF), between the two stations (Shapiro and Campillo, 2004; Sabra *et al.*, 2005). Therefore, the phase information of the IRF closely captures that of the true Green's function, in particular for surface waves, and has been widely used to image the Earth's structure (e.g., Shapiro *et al.*, 2005; Lin *et al.*, 2008). On the other hand, the amplitude information is, in theory, less reliable due to the data processing and the nonideal location of the ambient seismic field sources (Tsai, 2011; Weaver, 2011; Stehly and Boué, 2017). Nevertheless, several empirical and numerical studies have shown promising results in retrieving reliable attenuation measurement (Lawrence and Prieto, 2011; Lawrence *et al.*, 2013) and in simulating earthquake ground motions (e.g., Prieto and Beroza, 2008; Viens *et al.*, 2017).

Seismic interferometry with deconvolution has been used to successfully simulate the long-period ground shaking from earthquakes in different geological and tectonic contexts. The long-period seismic waves from moderate M_w 4–5 onshore earthquakes, in which the point-source approximation is valid at long periods, have been simulated in the United States (Prieto and Beroza, 2008; Denolle *et al.*, 2013; Sheng *et al.*, 2017) and Japan (Viens *et al.*, 2014). Kwak *et al.* (2017) also applied this technique to simulate the long-period waves generated by a mine collapse event (M_w 4.2) in South Korea. Large past and hypothetical future crustal earthquakes, in which finite faults need to be taken into account, have also been simulated (Denolle *et al.*, 2014; Viens, Miyake, *et al.*, 2016; Denolle *et al.*, 2018). Finally, the seismic interferometry technique has been shown to successfully recover 3D wave propagation effects in sedimentary basins, where the complex seismic wave propagation and amplification caused by the velocity structure is captured by the IRFs (Denolle *et al.*, 2014; Boué *et al.*, 2016; Viens, Koketsu, *et al.*, 2016). The simulation of long-period ground motions from subduction earthquakes with ambient seismic field IRFs, however, has only been the focus of one study (Viens *et al.*, 2015), due to the lack of offshore seismic networks. The deployment of ocean-bottom seismometers in subduction zones worldwide and the recent availability and accessibility of their data offer the opportunity to investigate the potential of seismic interferometry to simulate the long-period ground motions from large and megathrust earthquakes.

In southwest Japan, the subduction of the Philippine Sea plate beneath the Eurasian plate along the Nankai trough is well known to host M_w 8 and greater megathrust earthquakes about every 100–200 yr (Ando, 1975). To monitor the real-time seismic activity in this region, the Dense Oceanfloor Network System for Earthquakes and Tsunamis (DONET) was deployed by the Japan Agency for Marine-Earth Science and Technology (Kaneda *et al.*, 2015; Kawaguchi *et al.*, 2015). The DONET 1 network has been operational since 2011 and is composed of 20 stations with both broadband and strong-motion three-component sensors (Fig. 1). The most recent large events along the Nankai trough occurred in 2004 during the Off the Kii peninsula earthquake sequence, with an M_w 7.2 intraplate event that was followed 5 hr later by an M_w 7.5 intraplate earthquake. Although the DONET 1 network was not installed at the time of the earthquakes, the ground motions from these events were well recorded onshore by the different networks of the National Research Institute for Earth Science and Disaster Resilience (NIED; e.g., F-net, Hi-net, KiK-net, and K-NET; Okada *et al.*, 2004; Obara *et al.*, 2005). The recorded waveforms exhibit large long-period amplifications in the Osaka, Nagoya, and Kanto sedimentary basins (Miyake and Koketsu, 2005).

In this study, we focus on the simulation of long-period (4–10 s) ground motions from past and future potential offshore earthquakes along the Nankai trough using the ambient seismic field. First, we introduce the data and our methodology as well as the metrics that are used for quality assessment. We also briefly introduce the subduction-zone BC Hydro GMM developed by Abrahamson *et al.* (2016) that is used to cross-validate our results. We then simulate two

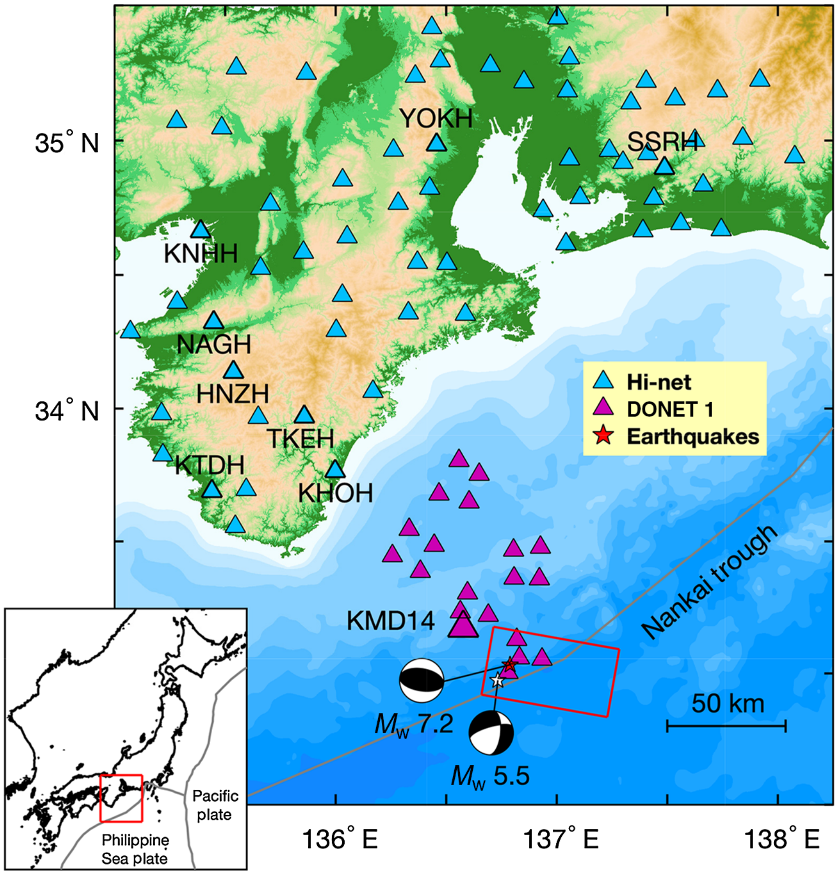

Figure 1. Topographic map of the Kii peninsula region and the Nankai subduction zone including the Hi-net and Dense Oceanfloor Network System for Earthquakes and Tsunamis (DONET 1) stations (triangles). The focal mechanisms of the 2004 M_w 5.5 and 7.2 earthquakes are shown together with their respective epicenters (stars). The contour of the fault plane of the 2004 M_w 7.2 event projected at the surface is shown by the rectangle. The KMD14 station is the virtual source station used to compute offshore–onshore impulse response functions (IRFs) and its location is shown by the large triangle. KMC10 and KMC11 stations are the closest stations from the epicenter of the M_w 5.5 event. The names of eight Hi-net stations used in this study are also indicated. (Inset) The Japan Islands and the rectangle is the region of interest. The color version of this figure is available only in the electronic edition.

earthquakes that occurred in 2004, a moderate M_w 5.5 event and the M_w 7.2 intraplate earthquake. We compare the simulated and observed long-period ground motions for these two events and cross-validate their spectral acceleration (SA) values with those from the GMM. Finally, we simulate a potential M_w 8.0 megathrust event that could occur along the Nankai trough, and compare the SA values of the predicted waveforms with those from the GMM.

Data and Methods

IRF Computation

We use four months of continuous data recorded from 1 June to 30 September 2015 by one DONET station (e.g., KMD14 station) and 60 Hi-net stations located in the surrounding area (Fig. 1). The study by Takagi *et al.* (2018) recently showed that the Pacific Ocean is the main source of surface waves during the summer season and that the Japan Sea generates most surface waves during winter months in the 4–8 s period band, which is similar to our focus on the 4–10 s period range. By selecting the data recorded during summer months, the distribution of ambient-noise sources favors the coherence of the signal from offshore to onshore paths near the Nankai trough, thus enhancing the quality of the IRFs.

The broadband seismometers of the DONET 1 network record continuous data with a 100 Hz sampling rate, and most sensors are buried in shallow 1-meter-deep boreholes. The Hi-net stations also record at 100 Hz and are located in boreholes with depths ranging between 100 and 3000 m. Although Hi-net seismometers are high-sensitivity sensors with a cutoff period of 1 s, reliable long-period (≥1 s) seismic waves can also be retrieved after correcting for the instrumental response thanks to the wide dynamic range of the recording system (Obara *et al.*, 2005). We correct the DONET and Hi-net data for their instrumental responses and rotate their horizontal components to the true north–south and east–west directions using the orientations determined by Nakano *et al.* (2012) and Shiomi (2013).

For each seismic station, we downsample the velocity data recorded by the three-component sensors to 10 Hz and divide them into 1-hour-long time series. To reduce the unwanted effects of transient signals from earthquakes, we discard the time windows with peaks greater than 10 times the standard deviation of the window. For each station pair, we compute the IRFs between the vertical, north, and east components using the deconvolution technique. This computation is performed in the frequency domain with a smoothing operator applied to the denominator spectrum using a moving average over 20 points. Additional details about the deconvolution method applied in this study can be found in Viens *et al.* (2017). The 1 hr IRFs are finally stacked together to improve the signal-to-noise ratio (SNR), time differentiated once to retrieve the proportionality between cross-correlation function and Green's function (Snieder, 2004; Roux *et al.*, 2005; Prieto *et al.*, 2011), and band-pass filtered between 4 and 10 s using a four-pole and two-pass Butterworth filter. We rotate the nine-component Green's tensor from the east–north–vertical (ENZ) coordinate system to the radial–transverse–vertical (RTZ) system for each station pair. By rotating the IRFs, we suppose that Rayleigh waves are retrieved on the Z–Z and R–R components and that Love waves are retrieved on the T–T component.

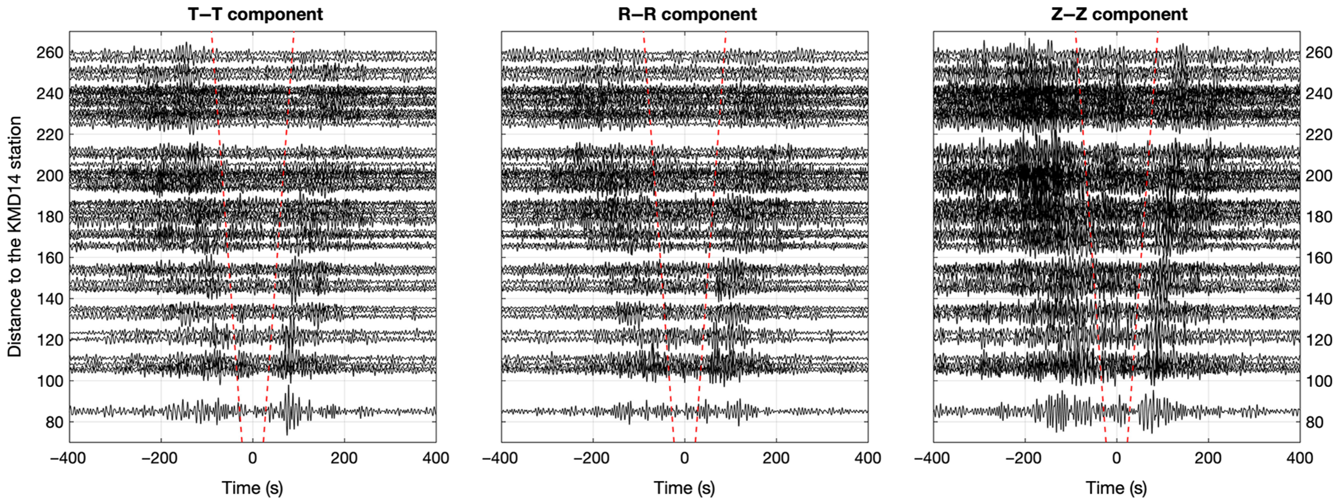

Figure 2. Causal (positive) and anticausal (negative) parts of the IRFs for the T–T, R–R, and Z–Z components as a function of the distance to the virtual source (KMD14). All waveforms are band-pass filtered between 4 and 10 s and dashed lines represent the 3.0 km/s moveout. The color version of this figure is available only in the electronic edition.

We show the IRFs for the T–T, R–R, and Z–Z components computed using the data recorded between June and September 2015 in Figure 2, and the six other components of the Green's tensor in Ⓔ Figure S1 (available in the supplemental content to this article). Propagating seismic waves can be observed on both anticausal (negative) and causal (positive) sides of the IRFs. As the amplitude of the causal part of the IRF is likely to better capture site amplification and attenuation effects than the anticausal part (Bowden *et al.*, 2015; Liu *et al.*, 2016), we only consider the causal part of the IRFs in this study. To characterize the potential bias of the IRF amplitudes caused by variations of ambient seismic field sources, we compute the SNR for the T–T, R–R, and Z–Z IRFs. The SNR is defined as the peak amplitude of the causal IRFs band-pass filtered between 4 and 10 s over the root mean square level of the 25 s preceding a velocity of 3.0 km/s for each station. The SNR values plotted against the azimuth from the virtual source (e.g., KMD14 station) are shown in Ⓔ Figure S2. Although there is almost no variation of the SNR with azimuth for the Z–Z component, there is some variation in the SNR of the R–R and T–T components. To reduce the amplitude biases, we first correct the IRF amplitudes for their surface-wave theoretical geometrical spreading (multiplication by $\sqrt{d_{v-r}}$, in which d_{v-r} is the virtual source–receiver distance) and show the peak values as a function of the azimuth from the virtual source in Ⓔ Figure S3. We then model the small azimuthal variations by fitting the peak amplitudes of the IRFs corrected for the surface-wave geometrical spreading with a third degree polynomial. We finally correct the IRF amplitudes by multiplying the waveforms by the ratio of the polynomial function value at the corresponding azimuths over the mean amplitude of the data.

Earthquake Data

For the M_w 5.5 and M_w 7.2 earthquakes considered in the following sections, earthquake records at Hi-net stations are first corrected for their instrumental responses to retrieve the velocity ground motion and the horizontal components are rotated to the true north–south and east–west directions using the orientations determined by Shiomi (2013). For each earthquake, the horizontal components are then rotated to R and T directions from the earthquake epicenter. Finally, the velocity data from the three components are downsampled to 10 Hz and band-pass filtered between 4 and 10 s using a four-pole and two-pass Butterworth filter.

Source Models

Moderate Earthquake Simulation. We first focus on the simulation of an M_w 5.5 earthquake, which occurred on 10 September 2004 at 11:05 a.m. (Japan Standard Time [JST]) at a depth of ~5 km (NIED centroid moment tensor solution). As mentioned in the IRF Computation section, the IRFs are computed between the KMD14 station, which is located ~26 km away from the epicenter in a shallow 1-meter-deep borehole, and onshore Hi-net stations. This allows us to retrieve better-quality IRFs than with the KMC10 and KMC11 stations, which are located closer to the epicenter but directly on the seafloor (Fig. 2 and Ⓔ Fig. S4). As mentioned in several studies (e.g., Stutzmann *et al.*, 2001; Crawford *et al.*, 2006), seismometers located directly on the seafloor are subject to additional noise sources, thus leading to a higher noise level, especially for the horizontal components (Ⓔ Fig. S5). Although some techniques have been developed to reduce the noise levels (Crawford and Webb, 2000), we leave this task to future work. To correct for the difference in location between the earthquake epicenter and the KMD14 virtual source, we simply time shift the IRFs considering a constant surface-wave velocity of 3.2 km/s, assuming that the surface-wave dispersion is weak in the narrow frequency band of interest. This value corresponds to ~90% of the average *S*-wave velocity in the upper 15 km of the crust following the Japan Integrated Velocity Structure Model (JIVSM, Koketsu *et al.*, 2009, 2012). We also correct the amplitude of the IRFs to account for the difference in surface-wave geometrical spreading between the virtual source–receiver (d_{v-r}) and the epicenter–receiver (d_{e-r}) distances (e.g., multiplication by $\sqrt{d_{v-r}}/\sqrt{d_{e-r}}$). Finally, we taper the IRFs to remove the spurious and nonphysical signals that appear to travel faster than 6 km/s and may contaminate the IRFs (e.g., Shapiro *et al.*, 2006; Zeng and Ni, 2010).

To simulate the velocity waveforms of a moderate earthquake, the T–T, R–R, and Z–Z IRFs are convolved with a source time function. For the M_w 5.5 event, which is approximated as a point source at the periods of interest, we use a triangle moment-rate function as the source time function. The duration of this function (T_r) is based on the moment-duration relation from Somerville *et al.* (1999) that is defined as $T_r = 2.03 \times 10^{-9} \times (m_0/10^7)^{(1/3)}$, in which m_0 is the seismic moment of the M_w 5.5 event in $N \cdot m$. For this event, we obtain a source time function duration T_r of 0.26 s, which is rounded to 0.3 s given our 10 Hz sampling rate. The amplitude of the source time function is set so that its integral over its duration is equal to the seismic moment of the M_w 5.5 event (e.g., 2.22×10^{17} $N \cdot m$).

After convolving the IRFs with the source time function, the simulated velocity waveforms need to be calibrated with the earthquake velocity seismograms as only the relative, rather than absolute, IRF amplitude is retrieved from the ambient seismic field. A calibration factor for each component of the IRF (e.g., Z–Z, R–R, and T–T) but common to all stations is calculated as follows. First, the absolute value of the Fourier transform amplitude of both the recorded and simulated velocity waveforms for all the stations is computed. Then, the absolute values are averaged over the 4–10 s period range and over the number of stations for both the recorded and simulated waveforms. Finally, the calibration factor is computed as the ratio of the observed over simulated values, similarly as in Viens *et al.* (2014). For each component, the simulated velocity waveforms are multiplied by their respective calibration factor. The calibration factors computed using the M_w 5.5 event for each component are used to calibrate the IRFs for the computation of large earthquakes in the following sections.

Radiation pattern effects matter when simulating ground motions at a wide range of source–receiver paths, in particular when the paths sample the nodal planes of the radiation pattern. Denolle *et al.* (2013) proposed to correct the surface impulse responses to the displacements that are radiated from a buried double-couple point source for moderate and shallow Californian earthquakes. For the M_w 5.5 earthquake of interest, the observed ground motions do not exhibit clear azimuthal variations that would be indicative of radiation pattern effects in the 4–10 s period range. To demonstrate this feature, we first correct the simulated and observed waveforms for the surface-wave geometrical spreading by multiplying them by $\sqrt{d_{e-r}}$. For the three components, we show the simulated and observed long-period peak ground velocity (PGV) values after surface-wave geometrical spreading correction as a function of the azimuth from the epicenter in Figure 3a and 3b, respectively. These values are computed for waves traveling slower than 3.0 km/s to reduce the effect of body waves and primarily focus on surface waves. We also compute the theoretical surface-wave (both Love and Rayleigh) amplitudes expected given the radiation pattern of the NIED moment tensor solution and the JIVSM profile near the earthquake source at various periods (Denolle *et al.*, 2013, their equations 13–15), and show them in Figure 3c.

In the 4–10 s period range, the theoretical Rayleigh-wave radiation pattern indicates that Rayleigh-wave amplitudes should increase from azimuth −60° to azimuth 20°. However, the observed vertical and radial long-period PGVs after geometrical spreading correction in Figure 3b do not exhibit such a variation. For the vertical component, the observed long-period PGVs even exhibit a decreasing trend with increasing azimuth angle. There is also no azimuthal variation of the simulated peak amplitudes of the R–R and Z–Z components in the 4–10 s period range. For the observed T and simulated using the T–T IRF amplitudes, the azimuthal variation is similar to the one expected from the Love-wave radiation pattern. However, because the simulated waveforms using the T–T IRFs only carry path information and no source effect, this variation must be attributed to wave propagation effects. At periods longer than 10 s, however, radiation pattern effects can be observed (Ⓔ Fig. S6). Nevertheless, although the loss of radiation pattern effects is possible at high frequencies, they have not been observed, to our best knowledge, at relatively long periods.

Our analysis may indicate that the accretionary wedge plays a dominant role in the wave propagation from offshore sources to onshore sites, in particular in the 4–10 s period range. The low sensitivity of the surface-wave amplitudes to source terms in the 4–10 s period range is interesting and deserves additional research that is beyond the focus of this study. Consequently, we choose not to use the correction term for focal mechanism effects proposed by Denolle *et al.* (2013). We simply use the Z–Z and R–R IRFs to simulate Rayleigh waves and the T–T IRFs to simulate Love waves, after accounting for the fact that the virtual source and the epicenter are not collocated, amplitude calibration, and convolution with the source time function of the M_w 5.5 event.

Large Earthquake Simulation. On 5 September 2004 at 19:07 (JST), an M_w 7.2 intraplate earthquake occurred along the Nankai subduction zone and was later recognized as the foreshock of an M_w 7.5 earthquake. Several studies investigated the rupture properties of the foreshock (Yagi, 2004; Park and Mori, 2005; Suzuki *et al.*, 2005; Bai *et al.*, 2007; Okuwaki and Yagi, 2018; Watanabe *et al.*, 2018), and we summarize their results in Table 1. Although the strike and dip angles of this earthquake are relatively consistent among the studies, the length, width, and hypocentral location vary significantly. The rupture velocity for this earthquake, which

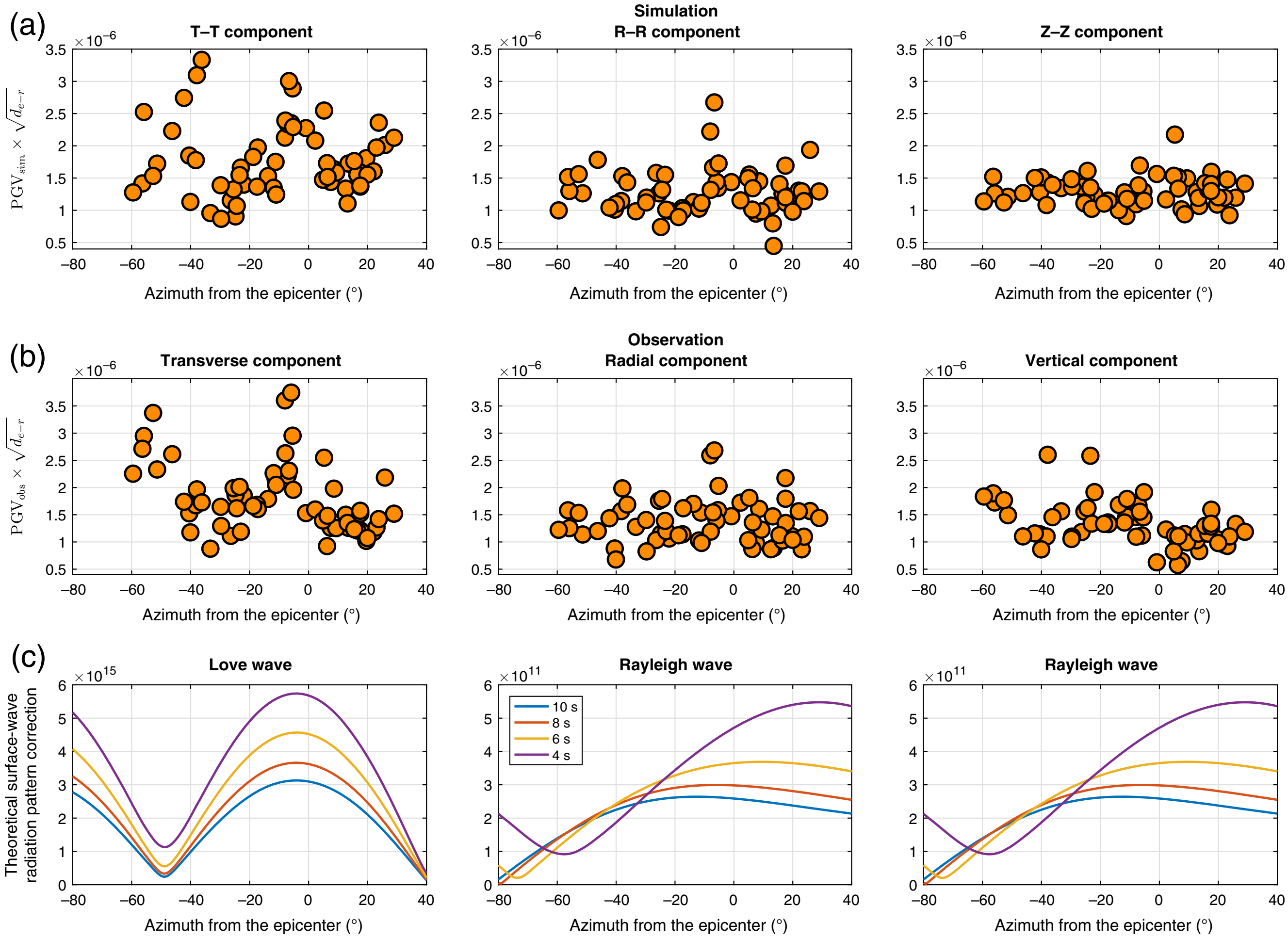

Figure 3. (a) Long-period peak ground velocity (PGV) of the simulated waveforms corrected for the surface-wave geometrical spreading ($\sqrt{d_{e-r}}$, in which d_{e-r} is the epicenter-to-receiver distance) as a function of the azimuth from the epicenter. The simulated waveforms are computed using the T–T, R–R, and Z–Z IRFs, after accounting for the fact that the virtual source and the epicenter are not collocated, amplitude calibration, and convolution with the source time function of the M_w 5.5 event. (b) Long-period PGV of the 2004 M_w 5.5 earthquake for the transverse, radial, and vertical components corrected for the surface-wave geometrical spreading ($\sqrt{d_{e-r}}$, in which d_{e-r} is epicenter-to-receiver distance) as a function of the azimuth from the epicenter location. All the PGVs in (a,b) are computed for waves traveling slower than 3.0 km/s to focus on surface-wave amplitudes. Zero azimuth is north. (c) Theoretical surface-wave amplitudes expected given the radiation pattern of the M_w 5.5 event and a local velocity profile taken near the source from the Japan Integrated Velocity Structure Model (Koketsu *et al.*, 2009, 2012). Both Love and Rayleigh theoretical amplitudes are shown at periods of 4, 6, 8, and 10 s. The color version of this figure is available only in the electronic edition.

is not systematically provided in the studies, is also poorly constrained. For example, the finite-fault source inversion study by Park and Mori (2005) found a rupture velocity of 2.0 km/s, whereas Suzuki *et al.* (2005) found a 3.0 km/s rupture velocity using an empirical Green's function approach. Such a large range of solutions is likely due to the sparsity of near-field measurements at the time of the earthquake (e.g., only the onshore stations in Fig. 1).

In this study, we set the length and width of the fault plane to 54 and 38 km, respectively, which is an average value among all the source inversion studies (Table 1). We discretize the fault plane into 27 by 19 subfaults of 2 by 2 km^2 area along the strike and dip directions, respectively. The surface projection of the fault plane on the seafloor is shown in Figure 4a. For each Hi-net station and each component, we attribute to each subfault an IRF that is calibrated to absolute levels with the calibration factor computed using the M_w 5.5 event. As the virtual source (KMD14) and the subfaults are not collocated, the IRFs are phase shifted with a constant surface-wave phase velocity of 3.2 km/s and are corrected for the difference of surface-wave geometrical spreading (e.g., multiplication by $\sqrt{d_{v-r}}/\sqrt{d_{mn-r}}$, in which d_{v-r} is the virtual source–receiver distance and d_{mn-r} is the surface projection of the mn subfault center–receiver distance). A cartoon of the configuration is shown in Figure 4d.

To account for the slip rate at each subfault, we use a triangle source time function for the moment-rate function (Fig. 4b). As we consider a somewhat elliptic slip model (Fig. 4a), the amplitude of the triangle moment-rate function varies throughout the fault with a maximum slip near the

Table 1
Source Parameters of the 2004 M_w 7.2 Off the Kii Peninsula Earthquake from Source Inversion Studies and Those Used in This Study

Study	M_w M_0 in $N \cdot m$	Latitude (°N), Longitude (°E), Hypocentral Depth (km)	Fault Size $L \times W$ (km^2)	Strike/Dip (°)
Yagi (2004)	7.2 7.0×10^{19}	33.06, 136.64, 18.3	66×30	280/42
Park and Mori (2005)	7.3 10×10^{19}	33.03, 136.80, 20	50×47	270/40
Suzuki *et al.* (2005)	7.1 7.7×10^{19}	33.03, 136.80, 37.6	30×15	263/55
Bai *et al.* (2007)	7.2 7.7×10^{19}	33.06, 136.64, 18.3	50×30	280/40
Okuwaki and Yagi (2018)	7.3 N/A	33.033, 136.798, 15	55×35	277/38
Watanabe *et al.* (2018)	7.2 N/A	32.86, 136.96, 5.4	35×20	280/40
This study	7.2 7.54×10^{19}	33.033, 136.798, 18.2	54×38	280/40

epicenter to respect the finite-fault and crack models. To determine the duration of the moment-rate function, which is constant over the fault plane, we vary it between 1.6 and 2.2 s every 0.1 s as the rise time for an M_w 7.2 earthquake is found to be around 1.9 s by Somerville *et al.* (1999). Finally, the triangle function for each subfault is time shifted considering the epicenter–subfault distance and assuming a constant rupture velocity. To account for the fact that the rupture velocity is not well constrained, we vary it between 2.0 and 3.4 km/s, every 0.1 km/s. The integral of the total source time function of the M_w 7.2 event (Fig. 4c) is equal to its seismic moment (e.g., $M_0 = 7.54 \times 10^{19}$ N · m, NIED centroid moment tensor solution).

The long-period ground motions of the 2004 M_w 7.2 earthquake are finally computed by summing all individual amplitude-calibrated IRFs convolved with their respective subfault moment-rate functions over the fault plane. The best results, which are shown in the Results section, are found for a rise time of 1.6 s for the triangle functions and a rupture velocity close to 3.1 km/s. These results are determined using a metric, which minimizes the SA residuals computed between the simulated and observed waveforms (e.g., the Waveform Comparison section). The results and details about the metric are provided in the Ⓔ supplemental content and in Figure S7. The rupture velocity parameter is not well constrained as the metric shows similar results for rupture velocities ranging from 2.8 to 3.4 km/s. Nevertheless, a rupture velocity of 3.1 km/s is consistent with the one found by Suzuki *et al.* (2005).

Finally, and similar to the M_w 5.5 event, we do not observe any clear radiation pattern effect for the M_w 7.2 intraplate earthquake in the 4–10 s period range (Ⓔ Fig. S8). Therefore, we do not use any focal mechanism correction to simulate the M_w 7.2 event. Radiation pattern effects are observed at longer periods (Ⓔ Fig. S8).

Virtual Megathrust Event Simulation. The probability of a megathrust (M_w 8+) earthquake occurring along the Nankai trough within the next 30 yr of 1 January 2013 is estimated as 60%–70% by The Headquarters for Earthquake Research Promotion (2013). To predict the long-period ground motions that could be generated by such an earthquake, we construct the fault plane of an M_w 8.0 scenario earthquake. The empirical scaling relations for reverse oceanic faulting developed by Blaser *et al.* (2010) suggest that the length and width of the fault plane are 142 and 66 km, respectively. We divide the fault plane into 2343 subfaults of 2 by 2 km^2 and set the strike and dip angles to 245° and 20°. The amplitude-calibrated IRFs computed between the KMD14 station and Hi-net stations are interpolated for each subfault in the same manner as for the M_w 7.2 event. The epicenter of the hypothetical earthquake is chosen to be in the middle of the fault plane and we consider an elliptic slip model (Fig. 5a), which is the solution to a uniform stress-drop crack (Eshelby, 1957), with triangle moment-rate functions. The amplitude of the triangle functions depends on the subfault's location and their duration (rise time) is set to 4.5 s (Somerville *et al.*, 1999). For this event, we consider three different rupture velocities of 2.0, 2.5, and 3.0 km/s and show their total moment-rate functions in Figure 5b. The integral of each total moment-rate function is equal to the seismic moment of an M_w 8.0 earthquake (e.g., $M_0 = 1.12 \times 10^{21}$ N · m). The velocity waveforms are simulated by summing the amplitude-calibrated IRFs convolved with their respective moment-rate functions over the fault plane, similar to the simulation of the M_w 7.2 event.

Validation: GMM for Subduction-Zone Earthquakes

In addition to comparing our results with the recorded waveforms, we also cross-validate them with the BC Hydro GMM for subduction zones (Abrahamson *et al.*, 2016). This GMM has been developed for horizontal-component acceleration spectral values using ground-motion records

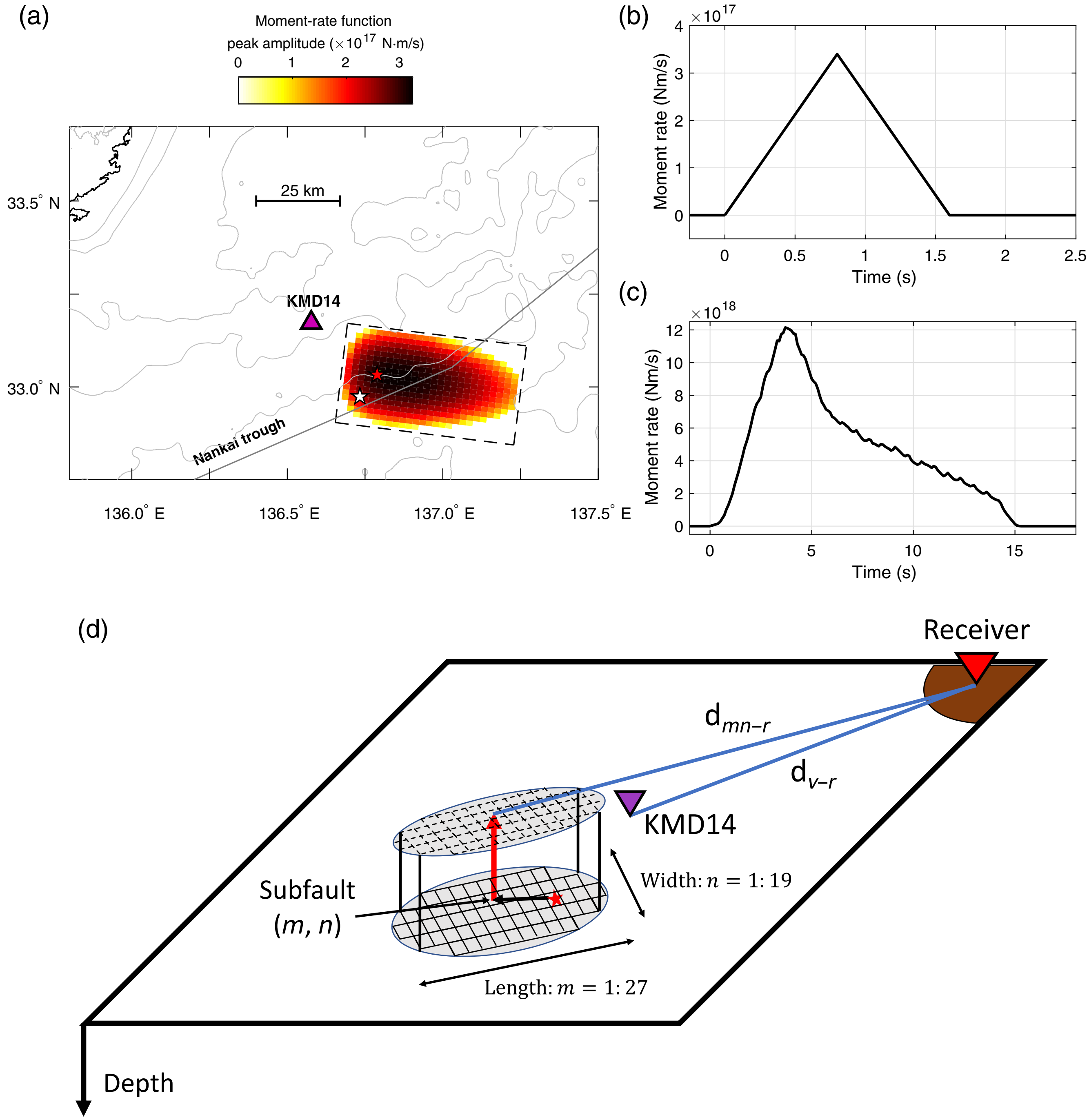

Figure 4. (a) Map of the region around the M_w 7.2 earthquake including the virtual source station (KMD14). The fault plane of the 2004 M_w 7.2 event projected at the surface is shown by the dashed rectangle. The area inside the fault plane represents the peak amplitude of the triangle moment-rate function shown in (b). The epicenter of the 2004 M_w 7.2 event is marked by a red star and corresponds to the subfault where the rupture is initiated in the simulations. The epicenter of the M_w 5.5 aftershock is shown by a white star. (b) Triangle moment-rate function near the epicenter with a duration of 1.6 s. Note that the amplitude of the triangle function depends on the location of the subfault and its onset depends on the rupture propagation. (c) Total moment-rate function for the simulated waveforms considering a rupture velocity of 3.1 km/s. The cumulative moment of the moment-rate function is equal to 7.54×10^{19} N · m, which corresponds to the seismic moment of an M_w 7.2 event. (d) Schematic representation of the large event simulation including the different distances used in the simulations. The fault plane is shown in gray together with its projection at the surface and the hypocenter is shown by the star. The virtual source station (KMD14) and a receiver located onshore are shown by the inverse triangles, respectively. d_{v-r} is the virtual source-to-receiver distance and d_{mn-r} is the (m, n) subfault-to-receiver distance. The color version of this figure is available only in the electronic edition.

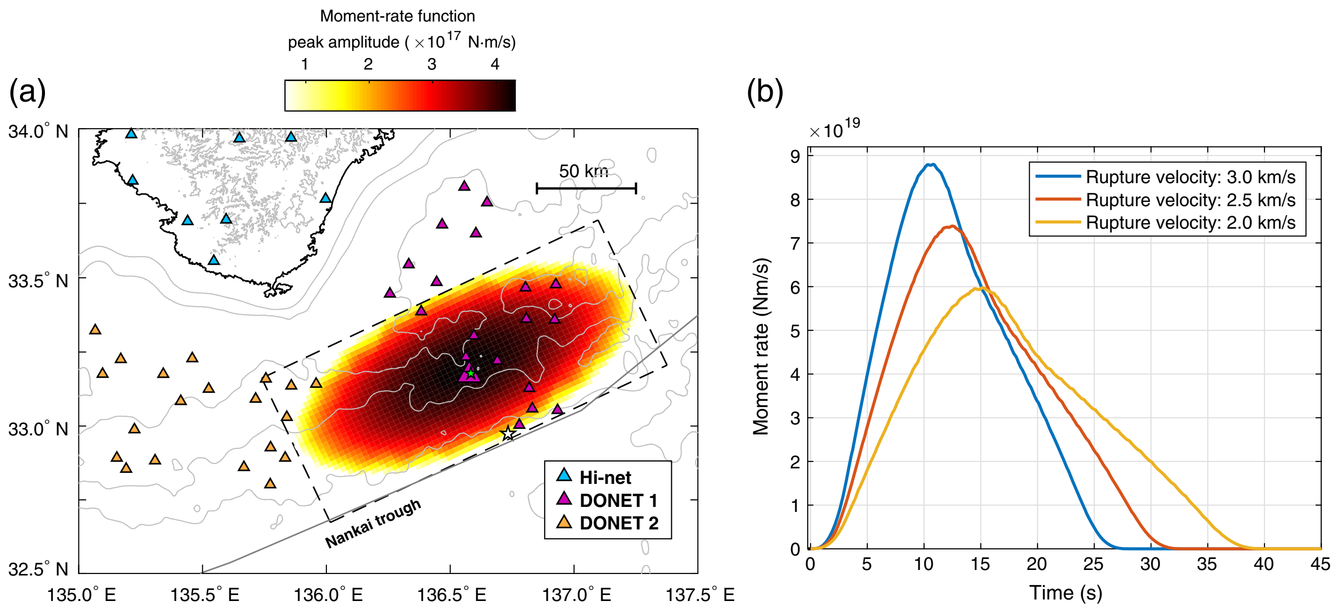

Figure 5. (a) Map of the Nankai subduction zone including the fault plane of a virtual M_w 8.0 earthquake (dashed rectangle) determined using the oceanic reverse-faulting scaling relationships from Blaser *et al.* (2010). The area inside the fault plane represents the peak amplitude of the triangle moment-rate function used for each subfault. The virtual source station (e.g., KMD14 station) is shown by the large triangle and the other DONET 1 stations, 20 of 29 DONET 2 stations, and a few Hi-net are represented by triangles. The star near the KMD14 station is the epicenter of the M_w 8.0 event and the epicenter of the M_w 5.5 event is shown by a white star. (b) Total moment-rate functions for rupture velocities of 2.0, 2.5, and 3.0 km/s. The color version of this figure is available only in the electronic edition.

from worldwide subduction-zone earthquakes, including Japanese earthquakes. In this section, we briefly describe the different parameters considered in our study and refer the reader to the original paper (e.g., Abrahamson *et al.*, 2016) for additional details.

The BC Hydro GMM is composed of two functional forms that have been determined from the regression analysis of records from interface and intraplate earthquakes. For the 2004 M_w 7.2 earthquake, we use the intraslab event functional form and consider that our stations are located in the fore-arc region. The intraslab GMM has a site amplification component that is based on V_{S30}, the average S-wave velocity in the upper 30 m of the ground. As Hi-net stations are located in relatively deep boreholes (100–3000 m depth), we use the borehole information provided on the KiK-net website to determine the S-wave velocity in the borehole at the depth of each station, and set the V_{S30} parameter to this value. The average S-wave velocity in the boreholes over the 60 Hi-net stations is 1458 m/s. For the stations with S-wave velocities higher than 1000 m/s, the V_{S30} parameter is set to 1000 m/s following the GMM formulation. For intraslab events, the BC Hydro model also considers the hypocentral distance, which is set accordingly to the hypocentral location in Table 1. To estimate the epistemic uncertainty in the median ground motion related to the break in magnitude scaling for M_w 8+ events, Abrahamson *et al.* (2016) introduced the $\Delta C1$ term, which is set to −0.3 for intraplate events.

For the virtual M_w 8.0 megathrust earthquake, the interface event functional form of the BC Hydro GMM is considered. We also consider that all stations are located in the fore-arc region and use the same site conditions as for the intraplate event. The distance parameter of the interface functional form is the closest distance between site and fault plane. Therefore, we set this distance to be the distance between each receiver station and the center of the closest subfault. For interface events, we use values of $\Delta C1$ of −0.4, −0.2, and 0.0 to capture the model's epistemic uncertainties as recommended by Abrahamson *et al.* (2016).

Waveform Comparison

To compare the simulated and observed waveforms, we use several metrics that quantify the differences in phase, amplitude, and response spectra. The correlation coefficient (CC) allows us to compare seismic phases and is computed for each component as

$$\mathrm{CC} = \frac{\sum_{t=N_{2.5}}^{N_{92.5}} S_t \times E_t}{\sqrt{\sum_{t=N_{2.5}}^{N_{92.5}} S_t^2 \times \sum_{t=N_{2.5}}^{N_{92.5}} E_t^2}}, \qquad (1)$$

in which E_t and S_t are the observed and simulated velocity waveforms, respectively. $N_{2.5}$ and $N_{92.5}$ correspond to the times at which 2.5% and 92.5% of the cumulative energy of both signals (sum of the time-series values squared) is reached. We allow a 2 s time shift of the simulated waveforms to maximize CC as the locations of the M_w 5.5 and M_w 7.2 earthquakes are not well constrained (e.g., distances between the epicenter of the M_w 7.2 event used in this study and those listed in Table 1 vary between 3.5 and 40 km). Additional work, which is not the scope of the study, could use this fitting approach to do earthquake relocation.

The amplitude difference between the simulated and observed waveforms is evaluated by computing the residuals of the long-period (4–10 s) PGVs for each component as

$$R_j = \ln\left(\frac{\mathrm{PGV}_{\mathrm{sim}_j}}{\mathrm{PGV}_{\mathrm{obs}_j}}\right), \qquad (2)$$

in which $\mathrm{PGV}_{\mathrm{obs}}$ and $\mathrm{PGV}_{\mathrm{sim}}$ are the observed and simulated long-period PGVs at the jth station, respectively, and ln is the natural logarithm.

We finally compute the 5% damped SA values for the observed and simulated waveforms at periods between 4 and 10 s. The velocity time series are first differentiated once in time to retrieve the corresponding acceleration waveforms and their response spectra are computed using the Duhamel's integral technique (Chopra, 2015). For each period τ_i and each component, we compute the residuals between the observed and simulated SA values $B_j(\tau_i)$ as

$$B_j(\tau_i) = \ln\left(\frac{\mathrm{As}_j(\tau_i)}{\mathrm{Ae}_j(\tau_i)}\right), \qquad (3)$$

in which Ae_j and As_j are the observed and simulated SA values at the jth station, respectively. The mean of the SA residuals is computed by averaging the residuals over the considered number of stations N (e.g., 60 stations) as

$$M(\tau_i) = \frac{1}{N}\sum_{j=1,N} B_j(\tau_i). \qquad (4)$$

To quantify the variability of the mean of the SA residuals, we also compute the 90% confidence interval and the one standard deviation to the mean for each component and each period.

As the BC Hydro GMM was developed for the SA of horizontal components, we compute the geometric mean of the horizontal components for the observed ($H_e(\tau)$) and simulated ($H_s(\tau)$) SA values at each period τ as

$$H_e(\tau) = \sqrt{\mathrm{Ae}^{\mathrm{T}}(\tau) \times \mathrm{Ae}^{\mathrm{R}}(\tau)}$$
$$H_s(\tau) = \sqrt{\mathrm{As}^{\mathrm{T}}(\tau) \times \mathrm{As}^{\mathrm{R}}(\tau)}, \qquad (5)$$

in which $\mathrm{Ae}^{\mathrm{T}}(\tau)$, $\mathrm{Ae}^{\mathrm{R}}(\tau)$, $\mathrm{As}^{\mathrm{T}}(\tau)$, and $\mathrm{As}^{\mathrm{R}}(\tau)$ are the observed (Ae) and simulated (As) SA values at a specific period τ with the component indicated by the superscript, with T for transverse and R for radial.

As the SA values of the BC Hydro GMM are in units of g, we simply multiply them by the standard gravity value (e.g., 980.665 $\mathrm{cm/s^2}$) to retrieve the corresponding values in $\mathrm{cm/s^2}$. The residuals between the geometric mean of the observed and simulated SA waveforms as well as the residuals between the GMM values and the geometric mean of the observed SA waveforms are then computed using equation (3) and averaged using equation (4).

Results

Simulation of the 2004 M_w 5.5 Event

We show the simulated and observed velocity waveforms in the 4–10 s period range for five stations located in the direction of Osaka city from the earthquake source (location in Fig. 1) in Figure 6a–c. At these stations, the waveforms exhibit relatively strong and elongated long-period surface waves compared to those from moderate crustal earthquakes in California (Denolle *et al.*, 2013) and Japan (Viens, Miyake, *et al.*, 2016). Because of the long duration of the ground motions, the CCs between the simulated and observed waveforms tend to be low, but the main wave packets can generally be retrieved for the three components. For the five stations shown in Figure 6a–c, the simulated and observed long-period PGVs agree relatively well. There is almost no basin amplification at the KNHH station as the station is located in a 2-kilometer-deep borehole on the bedrock of the Osaka basin. Finally, the simulated waveforms are mainly composed of surface waves and do not reproduce well the body waves from the earthquake (e.g., waves traveling faster than 3.0 km/s). However, in the 4–10 s period range and at relatively large distances from the epicenter, body waves tend to have smaller amplitudes than surface waves as shown in Figure 6a–c. This feature can be explained by a stronger geometrical spreading of body waves compared to surface waves as well as a stronger effect of the accretionary wedge on surface waves as shown by physics-based simulations (e.g., Furumura *et al.*, 2008; Yoshimura *et al.*, 2008; Guo *et al.*, 2016).

Over the 60 Hi-net stations, the residuals of the long-period PGVs computed using equation (2) are distributed around zero (mean values of 0.00, −0.07, and 0.00) and their standard deviations to the mean are relatively low with values of 0.35, 0.26, and 0.35 for the transverse, radial, and vertical components, respectively (Fig. 6d–f). Moreover, for the 60 Hi-net stations and the three components, 175 ratios between observed and simulated long-period PGVs (e.g., $\mathrm{PGV_{sim}/PGV_{obs}}$) are within a factor of 2, and only 5 ratios exhibit values beyond 2 but within a factor of 3. This suggests that the long-period PGVs are relatively well simulated for this earthquake. Finally, there are slight variations with distance of the long-period PGV residuals for the transverse and vertical components for distances shorter than 175 km from the virtual source. A possible explanation for this bias is that the surface-wave geometrical spreading correction scheme applied to the IRFs is not appropriate for short distances. Another explanation is that the earthquake location is not accurate. Nevertheless, the average path may become more similar for longer distances and yields a distribution of the long-period PGV residuals around the zero bias for the three components.

The 5% damped acceleration spectra of the simulated and observed waveforms for the three components at three stations (e.g., SSRH, YOKH, and KTDH, location in Fig. 1)

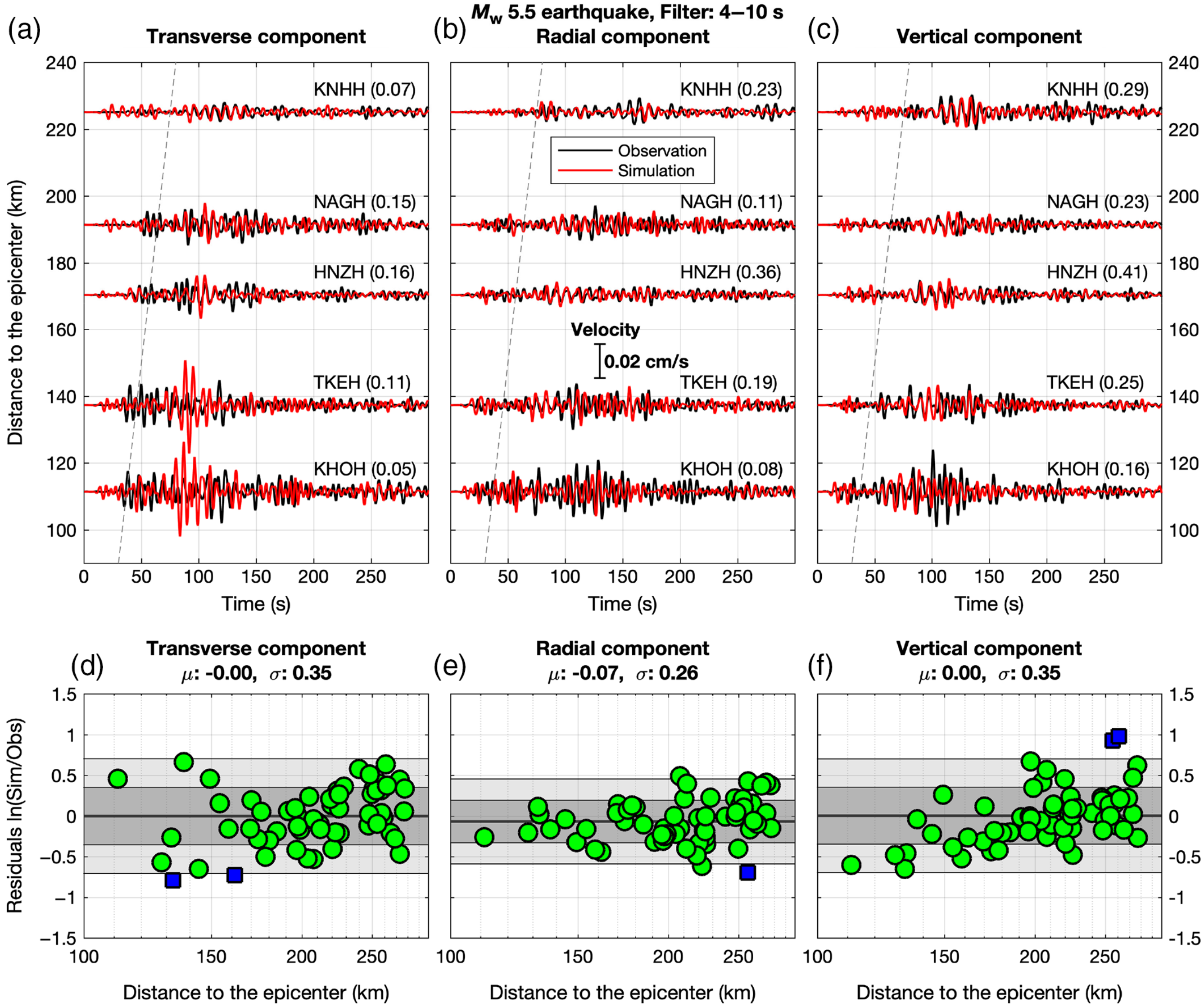

Figure 6. Comparison between the simulated and observed velocity waveforms for the (a) transverse, (b) radial, and (c) vertical components for five stations located in the source-to-Osaka city axis (location in Fig. 1). All the waveforms are band-pass filtered between 4 and 10 s. For each station, the correlation coefficient (CC) between the waveforms is indicated within parenthesis. Gray dashed lines represent the 3.0 km/s moveout. (d–f) Long-period PGV residuals computed using equation (2) for the (d) transverse, (e) radial, and (f) vertical components as a function of the distance to the epicenter. Circles indicate that the ratio between the simulated and observed PGVs is within a factor of 2 and the squares represent ratio values larger than a factor of 2 but within a factor of 3. The black thick line is the mean of the data, and the 1 and 2 standard deviations to the mean are shown by the dark gray and light gray areas, respectively. For each panel, the mean of the residuals (μ) and the standard deviation to the mean (σ) value are also indicated. The color version of this figure is available only in the electronic edition.

are shown in Figure 7a–c. We selected these stations to sample different azimuths from the epicenter. For these stations, the simulations reproduce relatively well the observed SAs in the 4–10 s period range. The acceleration spectra computed from the observed and simulated waveforms are more complex than those from the BC Hydro GMM. For each component, we compute the mean of the SA residuals over the 60 Hi-net stations and show it together with the 90% confidence interval and one standard deviation to the mean values in Figure 7d. In the 4–10 s period range, the mean is generally distributed around zero despite small but nonnegligible variations. However, the zero bias is always within one standard deviation to the mean, indicating that the simulated waveforms reproduce relatively well the long-period ground motions generated by the M_w 5.5 earthquake.

Simulation of the 2004 M_w 7.2 Earthquake

Using the same illustration as for the M_w 5.5 earthquake, we show the comparison between the velocity waveforms for the 2004 M_w 7.2 earthquake in Figure 8a–c. Similar to the

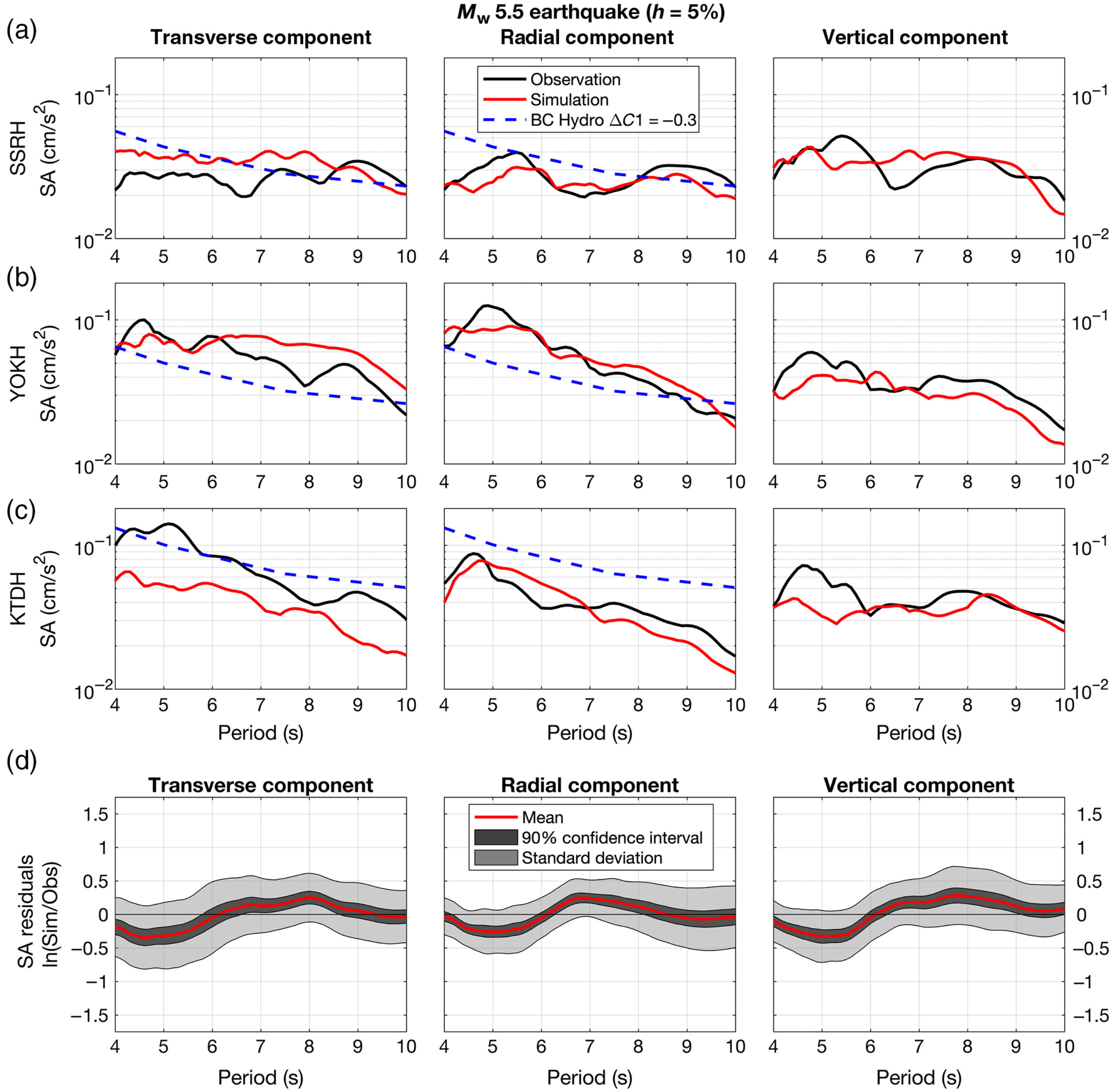

Figure 7. Simulated and observed 5% damped acceleration spectra for the M_w 5.5 earthquake at the (a) SSRH, (b) YOKH, and (c) KTDH stations for the transverse, radial, and vertical components. For the two horizontal components, the intraplate functional form of the BC Hydro ground-motion model (GMM) considering the hypocenter-to-receiver distance and the site conditions at each station is shown by a dashed line. (d) Spectral acceleration (SA) residuals over the 60 Hi-net stations computed using equation (3) for the M_w 5.5 earthquake. For each panel in (d), the mean of the SA residuals is shown together with the 90% confidence interval to the mean (dark gray area) and the one standard deviation to the mean (light gray area). The zero bias line is highlighted with a black line. The color version of this figure is available only in the electronic edition.

moderate event, the duration of the strong long-period ground motions is relatively long for all the stations, and the CCs are relatively low due to the complex wave propagation through the accretionary prism. Nonetheless, the recorded wave packets with the largest amplitudes are generally well reproduced by the simulated waveforms. We show the residuals of the long-period PGVs for the 60 Hi-net stations as a function of the distance to the epicenter in Figure 8d–f. For the transverse, radial, and vertical components, the means of the residuals are 0.24, −0.01, and −0.09, and the standard deviations to the mean are 0.39, 0.34, and 0.34, respectively. Moreover, we no longer observe any trend in the residuals with the distance from the epicenter, indicating that the crude geometrical spreading correction was more problematic in

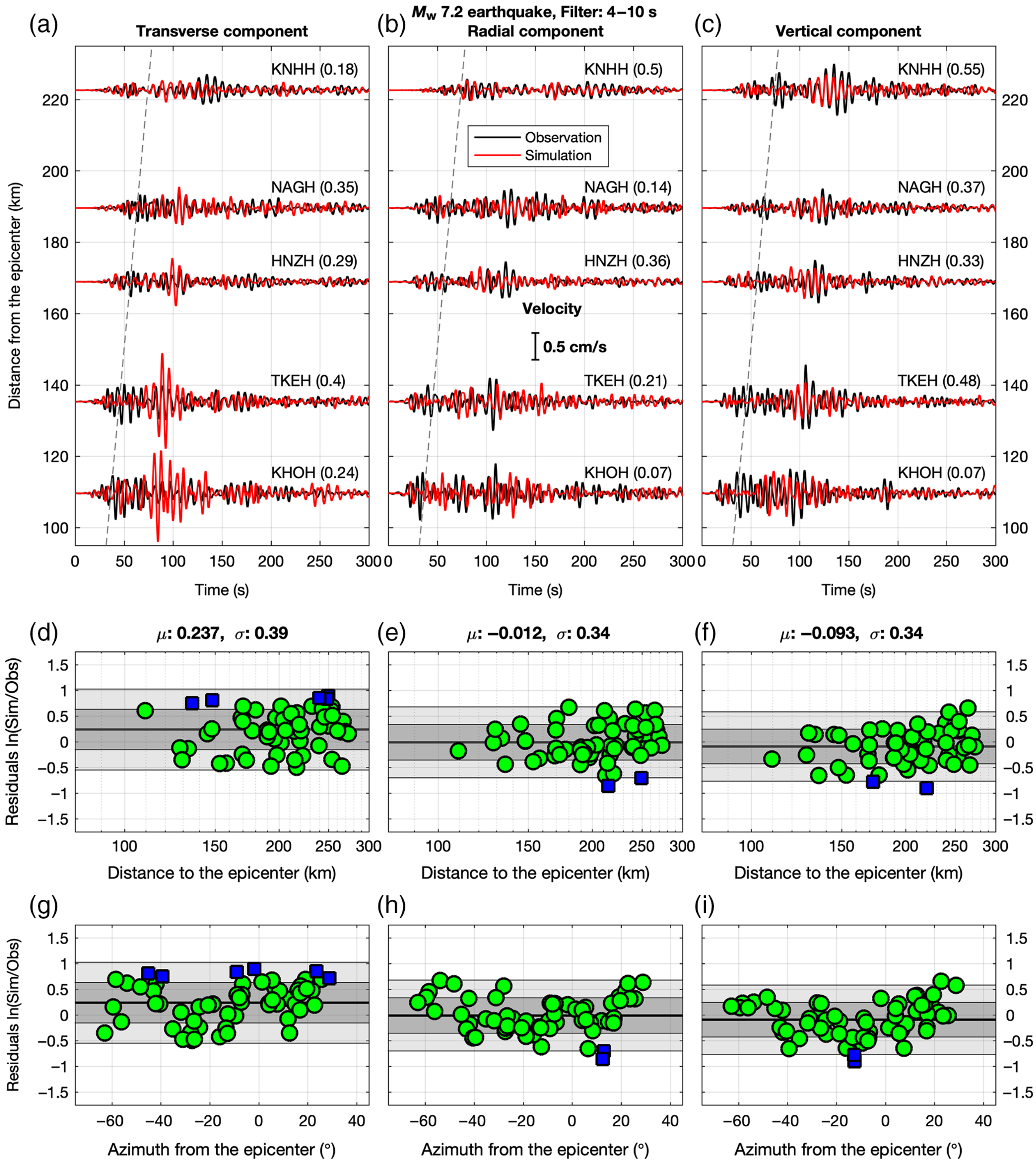

Figure 8. (a–f) Same as Figure 6a–f for the 2004 M_w 7.2 earthquake. (g–i) Long-period PGV residuals as a function of the azimuth from the epicenter (zero azimuth is north). Circles indicate that the ratio between simulated and observed PGVs are within a factor of 2 and the squares represent values larger than a factor of 2 but within a factor of 3. The color version of this figure is available only in the electronic edition.

the point-source case, but that the averaging over the fault plane reduces its effect. We also plot the residuals of the long-period PGVs as a function of the azimuth from the epicenter in Figure 8g–i to show the lack of systematic azimuthal variations. This indicates that the simple elliptic slip model used to simulate the long-period ground motions reproduces relatively well the observed ground motions of the large intraplate seismic event.

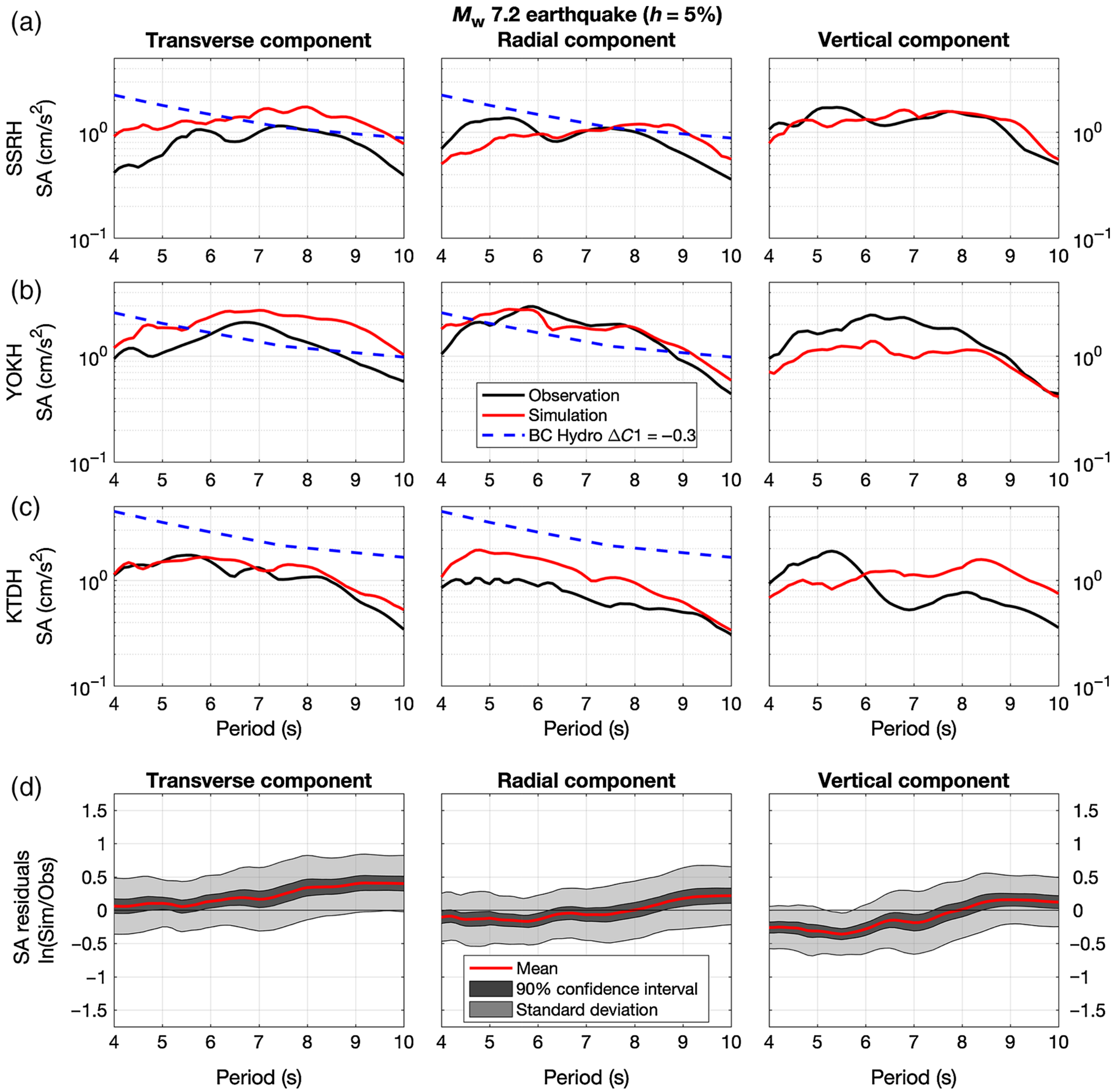

Figure 9. Same as Figure 7 for the 2004 M_w 7.2 earthquake. The color version of this figure is available only in the electronic edition.

We also show the SA values between 4 and 10 s for the three components at the SSRH, YOKH, and KTDH stations in Figure 9a–c. Similar to the M_w 5.5 event, the simulated and observed acceleration spectra for these three stations have similar shapes in the 4–10 s period range. Moreover, the acceleration spectra from the simulated waveforms reproduce better the observed ones compared to those from the BC Hydro GMM. We also show the SA residuals computed over the 60 Hi-net stations in Figure 9d for the three components. For the two horizontal components, the zero bias is within or close to the 90% confidence interval to the mean, and always within one standard deviation to the mean in the 4–10 s period range. For the vertical component, the average acceleration spectra of the simulated waveforms slightly underestimate those from the observed ground motions at periods between 5 and 6 s, because the zero bias is slightly outside one standard deviation to the mean. For periods longer than 6 s, the mean of the residuals becomes much closer to the zero bias.

In Figure 10, we show the residuals calculated between the observed and simulated SA values averaged over the two horizontal components using equation (5). The SA residuals are close to the zero bias as discussed earlier. We also show the residuals computed between the observed and GMM SA

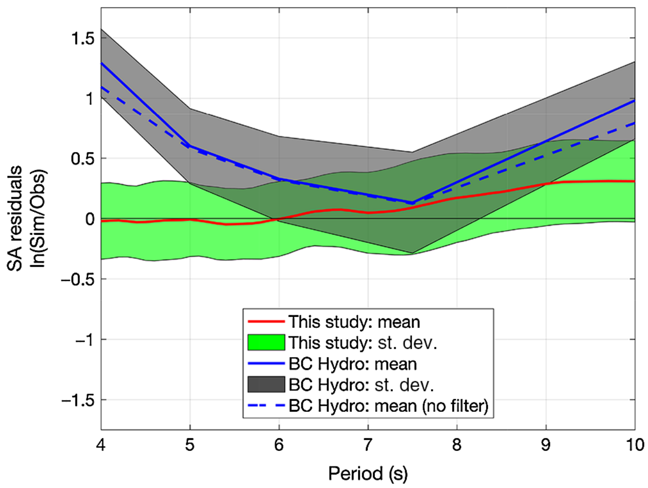

Figure 10. Comparison between the mean and the 1 standard deviation (st. dev.) to the mean of the SA residuals computed between the band-pass filtered M_w 7.2 earthquake records and the simulations and between the band-pass filtered M_w 7.2 earthquake records and the BC Hydro GMM. The mean of the SA residuals computed from the unfiltered 2004 M_w 7.2 earthquake records and the BC Hydro GMM is shown by the dashed line. The zero bias is highlighted with a black line. The color version of this figure is available only in the electronic edition.

values at discrete periods of 4, 5, 6, 7.5, and 10 s. The GMM does not perform well as the zero bias is outside one standard deviation to the mean for periods of 4 and 10 s, indicating that the GMM overpredicts the observed SA values at these periods. One of the reasons of this bias at periods of 4 and 10 s is the band-pass filter applied to the observed waveforms, which reduces the amplitude of the SA values at these periods. We also show in Figure 10 the mean of the SA residuals computed with unfiltered recorded waveforms. Although the effect of the band-pass filter is nonnegligible, the GMM SA values at 4 and 10 s still overpredict the observed unfiltered waveforms. Therefore, our simulations perform better than the BC Hydro GMM for the 2004 M_w 7.2 earthquake in the 4–10 s period range.

Long-Period Ground Motions from a Virtual M_w 8.0 Megathrust Event

Finally, we predict the long-period ground motions of a hypothetical M_w 8.0 subduction event for rupture velocities of 2.0, 2.5, and 3.0 km/s and show their horizontal waveforms at the KHOH and KNHH stations in Figure 11a–d. Unsurprisingly, the level of the long-period ground motion increases with the increasing rupture velocity, as expected that faster ruptures generate stronger ground motions.

We show the 5% damped SA values at 5, 6, and 7.5 s computed from the simulated waveforms for the three rupture velocities as a function of the distance from the closest subfault where slip occurred to each receiver station (equivalent to R_{rup} distance in the BC Hydro GMM) in Figure 11e–l. For the periods of interest, we observe a general decay of the SA values with increasing distance from the source and an increase of the SA values with increasing rupture velocity. We also show the SA values from the plate-interface event BC Hydro GMM in Figure 11e–l. As the rupture velocity is not accounted in the GMMs, the GMM predictions are invariant with respect to rupture velocity in this exercise. However, because this parametric function was determined from observed ground motions, it should account for realistic rupture velocities of megathrust events. Overall, the GMM SA values decay with increasing periods, whereas the virtual megathrust SA values remain constant, if not slightly amplified. This is consistent with the results for the M_w 7.2 earthquake, in which the simulated and observed waveforms remain constant with increasing periods from 5 to 7.5 s (Ⓔ Fig. S9). For a rupture velocity of 2.0 km/s, the SA values from our simulations are lower than those from the GMM at a period of 5 s, and comparable at periods of 6 and 7.5 s. For a 3.0 km/s rupture velocity, our simulations have SA values higher than those from the GMM for the three periods. For a rupture velocity of 2.5 km/s, a commonly reported value for subduction-zone earthquakes, the agreement between the SA values is good at 5 s and our simulations have higher values than the GMM at periods of 6 and 7.5 s. Therefore, for a hypothetical M_w 8.0 subduction event with a rupture velocity of 2.5 km/s or higher, our simulations show that the long-period ground motions at periods of 5, 6, and 7.5 are likely to be higher than those expected with the BC Hydro GMM.

The Hi-net stations are located in deep boreholes on the bedrock, and therefore a linear response of the surrounding material is expected. However, for stations located at the surface of sedimentary basins composed of almost cohesionless materials, one might expect a nonlinear response of the basin that could reduce long-period shaking levels as shown by the simulations performed by Roten *et al.* (2014).

Conclusions

In this study, we simulated the long-period ground motions of subduction-zone earthquakes using the ambient seismic field. We first retrieved IRFs between an offshore DONET station (KMD14) and onshore Hi-net stations using seismic interferometry by deconvolution. We then convolved the IRFs with a triangle source time function to simulate the velocity ground motions of a moderate M_w 5.5 earthquake, which is approximated as a point source. As only the relative amplitude of the IRFs is retrieved with the deconvolution technique, we computed a calibration factor for each component of the IRFs using the records of the M_w 5.5 event. After amplitude calibration, we compared the simulated and observed velocity waveforms and found that the observed ground motions do not carry the signature of any radiation pattern effects in the 4–10 s period range. This indicates that the long-period ground motions recorded onshore are likely more affected by the wave propagation through the accretionary wedge than by source effects. This feature allowed

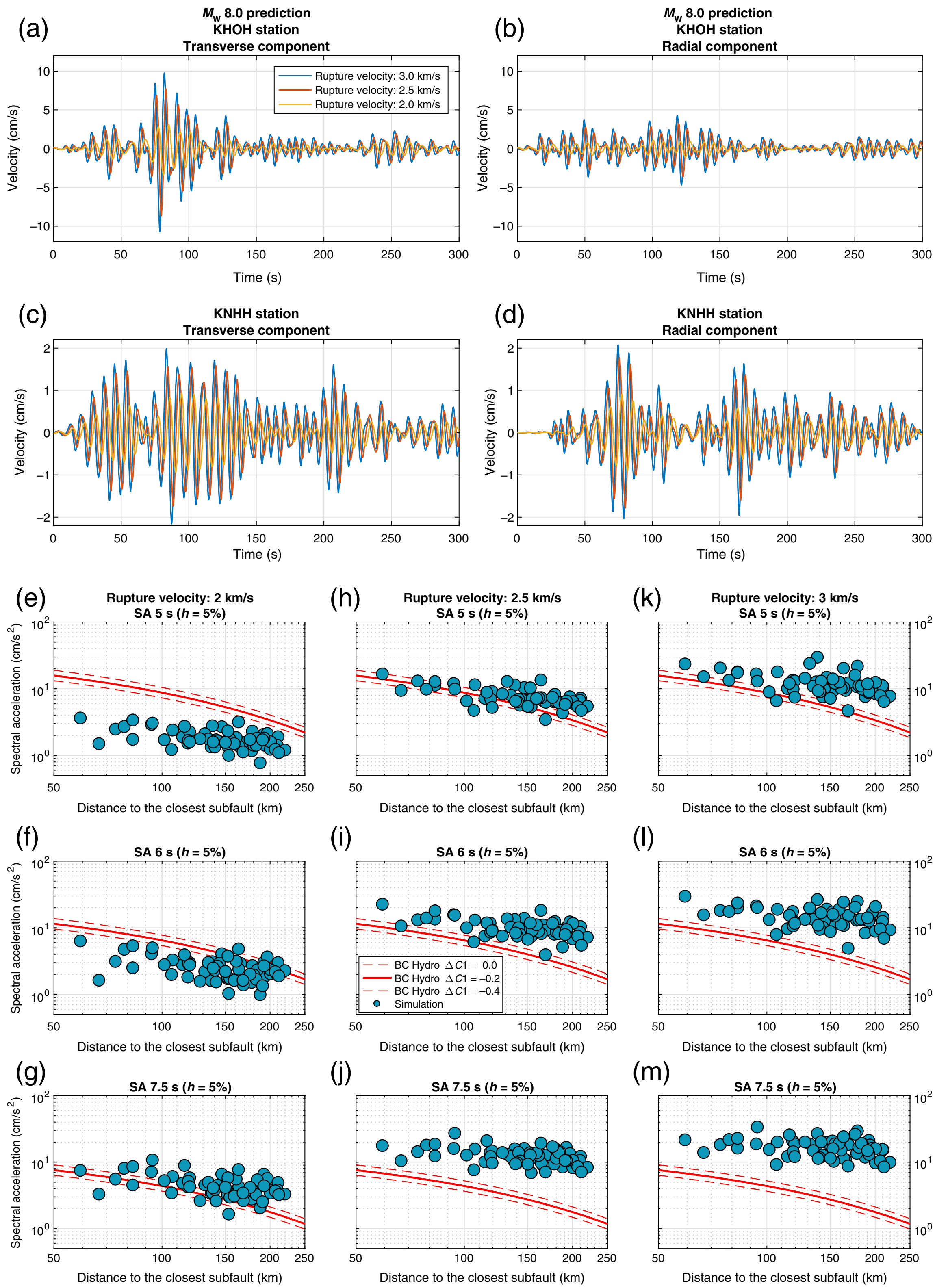

Figure 11. (a–d) Simulated velocity waveforms for the transverse and radial components at the KHOH and KNHH stations for a hypothetical M_w 8.0 subduction earthquake. For each panel, the waveforms are simulated considering constant rupture velocities of 2.0, 2.5, and 3.0 km/s. All waveforms are band-pass filtered between 4 and 10 s. (e–l) 5% damped SA values at periods of 5, 6, and 7.5 s from the median BC Hydro GMM (Abrahamson *et al.*, 2016) and from our simulations (circles) considering rupture velocities of (e–g) 2.0, (h–j) 2.5, and (k–m) 3.0 km/s for the hypothetical M_w 8.0 subduction earthquake. All the SA values are shown as a function of the distance to the closest subfault where slip occurs. For each panel, three values of the $\Delta C1$ parameter are shown for the BC Hydro GMM ($V_{S30} = 1000$ m/s), which are set to capture the epistemic uncertainties. The color version of this figure is available only in the electronic edition.

us to simplify the simulations and to generalize the predictions by simply using minimal transformation of the IRFs.

We further compared the simulated and observed velocity waveforms of the moderate M_w 5.5 intraplate earthquake using several metrics. We showed that the simulated and observed waveforms have similar wave packets and that long-period PGVs agree well in the 4–10 s period range. Moreover, the analysis of the SA values demonstrated that the spectral content of the observed and simulated waveforms is relatively similar in the period range of interest.

We then constructed a finite-fault elliptic slip source model of the 2004 M_w 7.2 intraplate earthquake, which was inspired by previously reported finite-fault inversions. By combining the amplitude-calibrated IRFs and the source model, we simulated the long-period ground motions of this event. For a constant rupture velocity of 3.1 km/s, our simulations reproduced well the observed waveforms in terms of phase, amplitude, and SA in the 4–10 s period range. We also cross-validated our results with the BC Hydro GMM and showed an improved performance in the predictions with our approach in the period range of interest.

We finally predicted the long-period ground motions of a hypothetical M_w 8.0 megathrust event that could occur along the Nankai subduction zone with an elliptic slip source model. Although the source model considered in this study is very simple, the SA values from the simulated waveforms using rupture velocities of 2.5 km/s or higher are larger than those computed from the BC Hydro GMM at periods of 5, 6, and 7.5 s. In future work, the simulations will be improved to better assess the seismic hazard related to the long-period ground motions from hypothetical megathrust events that could occur along the Nankai trough. This could be done by including multiple virtual source stations from the DONET 1 and 2 networks to better capture the 3D wave propagation from different parts of the fault. Moreover, realistic kinematic source models should be used to infer the long-period ground-motion variability related to M_w 8+ megathrust events in this region. Finally, future work should explore further data-processing techniques to improve the SNR of offshore–onshore IRFs, as ocean-bottom seismometer data have relatively high noise levels at periods longer than 5 s (Crawford and Webb, 2000; Webb and Crawford, 2010).

With the increasing number of offshore and onshore networks, the ambient seismic-field-based method could be applied to different subduction zones worldwide to simulate and predict the long-period ground motions of past and future megathrust earthquakes. For example, the Cascadia, Costa Rica, and Alaska subduction zones also benefit from multiyear offshore arrays that could be used to perform similar long-period ground-motion predictions of megathrust events. Such results could be coupled to those from other techniques such as physics-based simulations and GMMs to better assess seismic hazard related to offshore subduction earthquakes.

Data and Resources

Both the Hi-net and Dense Oceanfloor Network System for Earthquakes and Tsunamis (DONET) data can be downloaded at http://www.hinet.bosai.go.jp. Information about earthquakes is from the Japan Meteorological Agency (JMA) and F-net/National Research Institute for Earth Science and Disaster Resilience (NIED). The borehole data at Hi-net stations can be found on the KiK-net/NIED website at http://www.kyoshin.bosai.go.jp. The Python and MATLAB codes used in this study to compute the impulse response functions (IRFs), to simulate the M_w 7.2 event, and to compute acceleration response spectra are available at https://github.com/lviens. All websites were last accessed on May 2019.

Acknowledgments

The authors are grateful to Hiroe Miyake for helpful discussions about this study. The authors thank Associate Editor Arben Pitarka and two anonymous reviewers for their detailed and constructive comments. This work is supported by National Science Foundation (NSF) Award Number EAR-1663827. L. V. is currently supported by the Japan Society for the Promotion of Science Fellowship. The authors acknowledge the National Research Institute for Earth Science and Disaster Resilience (NIED) for providing the Hi-net data and Japan Agency for Marine-Earth Science and Technology (JAMSTEC) for the Dense Oceanfloor Network System for Earthquakes and Tsunamis (DONET) data. The authors also thank the Japan Meteorological Agency (JMA) and F-net/NIED for providing information about earthquakes, and KiK-net/NIED for the borehole information data. The authors are grateful to Ryo Okuwaki for providing the source model of the 2004 M_w 7.2 earthquake.

References

Abrahamson, N., N. Gregor, and K. Addo (2016). BC Hydro ground motion prediction equations for subduction earthquakes, *Earthq. Spectra* **32,** 23–44, doi: 10.1193/051712EQS188MR.

Anderson, J. G., P. Bodin, J. N. Brune, J. Prince, S. K. Singh, R. Quaas, and M. Onate (1986). Strong ground motion from the Michoacan, Mexico, earthquake, *Science* **233,** 1043–1049, doi: 10.1126/science.233.4768.1043.

Ando, M. (1975). Source mechanisms and tectonic significance of historical earthquakes along the Nankai trough, Japan, *Tectonophysics* **27,** 119–140, doi: 10.1016/0040-1951(75)90102-X.

Atkinson, G. M., and D. M. Boore (2003). Empirical ground-motion relations for subduction-zone earthquakes and their application to Cascadia and other regions, *Bull. Seismol. Soc. Am.* **93,** 1703, doi: 10.1785/0120020156.

Atkinson, G. M., and D. M. Boore (2008). Erratum to empirical ground-motion relations for subduction zone earthquakes and their application to Cascadia and other regions, *Bull. Seismol. Soc. Am.* **98,** 2567, doi: 10.1785/0120080108.

Bai, L., E. A. Bergman, E. R. Engdahl, and I. Kawasaki (2007). The 2004 earthquakes offshore of the Kii peninsula, Japan: Hypocentral relocation, source process and tectonic implication, *Phys. Earth Planet. In.* **165,** 47–55, doi: 10.1016/j.pepi.2007.07.007.

BC Hydro (2012). Probabilistic seismic hazard analysis (PSHA) model, *BC Hydro Engineering Report E658*, Vancouver.

Beck, J. L., and J. F. Hall (1986). Factors contributing to the catastrophe in Mexico City during the earthquake of September 19, 1985, *Geophys. Res. Lett.* **13,** 593–596, doi: 10.1029/GL013i006p00593.

Blaser, L., F. Krüger, M. Ohrnberger, and F. Scherbaum (2010). Scaling relations of earthquake source parameter estimates with special focus on subduction environment, *Bull. Seismol. Soc. Am.* **100,** 2914–2926, doi: 10.1785/0120100111.

Boué, P., M. Denolle, N. Hirata, S. Nakagawa, and G. C. Beroza (2016). Beyond basin resonance: Characterizing wave propagation using a dense array and the ambient seismic field, *Geophys. J. Int.* **206,** 1261–1272, doi: 10.1093/gji/ggw205.

Bowden, D. C., V. C. Tsai, and F. C. Lin (2015). Site amplification, attenuation, and scattering from noise correlation amplitudes across a dense array in Long Beach, CA, *Geophys. Res. Lett.* **42,** 1360–1367, doi: 10.1002/2014GL062662.

Chopra, A. (2015). *Dynamics of Structures*, International Edition, Pearson Education Limited, Harlow, United Kingdom.

Crawford, W. C., and S. C. Webb (2000). Identifying and removing tilt noise from low-frequency (<0.1 Hz) seafloor vertical seismic data, *Bull. Seismol. Soc. Am.* **90,** 952, doi: 10.1785/0119990121.

Crawford, W. C., R. A. Stephen, and S. T. Bolmer (2006). A second look at low-frequency marine vertical seismometer data quality at the OSN-1 site off Hawaii for seafloor, buried, and borehole emplacements, *Bull. Seismol. Soc. Am.* **96,** 1952, doi: 10.1785/0120050234.

Crouse, C. B., Y. K. Vyas, and B. A. Schell (1988). Ground motions from subduction-zone earthquakes, *Bull. Seismol. Soc. Am.* **78,** 1.

Denolle, M. A., P. Boué, N. Hirata, and G. C. Beroza (2018). Strong shaking predicted in Tokyo from an expected M7+ Itoigawa-Shizuoka earthquake, *J. Geophys. Res.* **123,** 3968–3992, doi: 10.1029/2017JB015184.

Denolle, M. A., E. M. Dunham, G. A. Prieto, and G. C. Beroza (2013). Ground motion prediction of realistic earthquake sources using the ambient seismic field, *J. Geophys.* **118,** 2102–2118, doi: 10.1029/2012JB009603.

Denolle, M. A., E. M. Dunham, G. A. Prieto, and G. C. Beroza (2014). Strong ground motion prediction using virtual earthquakes, *Science* **343,** 399–403, doi: 10.1126/science.1245678.

Eshelby, J. (1957). The determination of the elastic field of an ellipsoidal inclusion, and related problems, *Proc. Math. Phys. Sci.* **241,** 376–396, doi: 10.1098/rspa.1957.0133.

Furumura, T., T. Hayakawa, M. Nakamura, K. Koketsu, and T. Baba (2008). Development of long-period ground motions from the Nankai trough, Japan, earthquakes: Observations and computer simulation of the 1944 Tonankai (Mw 8.1) and the 2004 SE Off-Kii Peninsula (Mw 7.4) earthquakes, *Pure Appl. Geophys.* **165,** 585–607, doi: 10.1007/s00024-008-0318-8.

Guo, Y., K. Koketsu, and H. Miyake (2016). Propagation mechanism of long-period ground motions for offshore earthquakes along the Nankai trough: Effects of the accretionary wedge, *Bull. Seismol. Soc. Am.* **106,** 1176–1197, doi: 10.1785/0120150315.

Kaneda, Y., K. Kawaguchi, E. Araki, H. Matsumoto, T. Nakamura, S. Kamiya, K. Ariyoshi, T. Hori, T. Baba, and N. Takahashi (2015). Development and application of an advanced ocean floor network system for megathrust earthquakes and tsunamis, in *Seafloor Observatories*, P. Favali, L. Beranzoli, and A. De Santis (Editors), Springer Berlin Heidelberg, Berlin/Heidelberg, Germany, 643–662.

Kawaguchi, K., S. Kaneko, T. Nishida, and T. Komine (2015). Construction of the DONET real-time seafloor observatory for earthquakes and tsunami monitoring, in *Seafloor Observatories*, P. Favali, L. Beranzoli, and A. De Santis (Editors), Springer Berlin Heidelberg, Berlin/Heidelberg, Germany, 211–228.

Koketsu, K., K. Hatayama, T. Furumura, Y. Ikegami, and S. Akiyama (2005). Damaging long-period ground motions from the 2003 M_w 8.3 Tokachi-oki, Japan earthquake, *Seismol. Res. Lett.* **76,** 67–73, doi: 10.1785/gssrl.76.1.67.

Koketsu, K., H. Miyake, Afnimar, and Y. Tanaka (2009). A proposal for a standard procedure of modeling 3-D velocity structures and its application to the Tokyo metropolitan area, Japan, *Tectonophysics* **472,** 290–300, doi: 10.1016/j.tecto.2008.05.037.

Koketsu, K., H. Miyake, H. Fujiwara, and T. Hashimoto (2008). Progress towards a Japan integrated velocity structure model and long-period ground motion hazard map, *Proc. of the 14th World Conf. on Earthquake Engineering*, Beijing, China, 12–17 October 2008, S10–038.

Koketsu, K., H. Miyake, and H. Suzuki (2012). Japan integrated velocity structure model version 1, *Proc. of the 15th World Conf. on Earthquake Engineering*, Lisbon, Portugal, 24–28 September, 1773.

Kwak, S., S. G. Song, G. Kim, C. Cho, and J. S. Shin (2017). Investigating the capability to extract impulse response functions from ambient seismic noise using a mine collapse event, *Geophys. Res. Lett.* **44,** 9653–9662, doi: 10.1002/2017GL075532.

Lawrence, J. F., and G. A. Prieto (2011). Attenuation tomography of the western United States from ambient seismic noise, *J. Geophys. Res.* **116,** no. B06302, doi: 10.1029/2010JB007836.

Lawrence, J. F., M. Denolle, K. J. Seats, and G. A. Prieto (2013). A numeric evaluation of attenuation from ambient noise correlation functions, *J. Geophys. Res.* **118,** 6134–6145, doi: 10.1002/2012JB009513.

Lin, F.-C., M. P. Moschetti, and M. H. Ritzwoller (2008). Surface wave tomography of the western United States from ambient seismic noise: Rayleigh and Love wave phase velocity maps, *Geophys. J. Int.* **173,** 281–298, doi: 10.1111/j.1365-246X.2008.03720.x.

Liu, X., Y. Ben-Zion, and D. Zigone (2016). Frequency domain analysis of errors in cross-correlations of ambient seismic noise, *Geophys. J. Int.* **207,** 1630–1652, doi: 10.1093/gji/ggw361.

Miyake, H., and K. Koketsu (2005). Long-period ground motions from a large offshore earthquake: The case of the 2004 off the Kii peninsula earthquake, Japan, *Earth Planets Space* **57,** 203–207, doi: 10.1186/BF03351816.

Nakano, M., T. Tonegawa, and Y. Kaneda (2012). Orientations of DONET seismometers estimated from seismic waveforms, *JAMSTEC Rep. Res. Dev.* **15,** 77–89.

Obara, K., K. Kasahara, S. Hori, and Y. Okada (2005). A densely distributed high-sensitivity seismograph network in Japan: Hi-net by National Research Institute for Earth Science and Disaster Prevention, *Rev. Sci. Instrum.* **76,** 021301, doi: 10.1063/1.1854197.

Okada, Y., K. Kasahara, S. Hori, K. Obara, S. Sekiguchi, H. Fujiwara, and A. Yamamoto (2004). Recent progress of seismic observation networks in Japan—Hi-net, F-net, K-NET and KiK-net, *Earth Planets Space* **56,** xv–xxviii, doi: 10.1186/BF03353076.

Okuwaki, R., and Y. Yagi (2018). rokuwaki/2004Mw7.2KiiJapan: v1.0, doi: 10.5281/zenodo.1493833.

Park, S.-C., and J. Mori (2005). The 2004 sequence of triggered earthquakes off the Kii peninsula, Japan, *Earth Planets Space* **57,** 315–320, doi: 10.1186/BF03352569.

Prieto, G. A., and G. C. Beroza (2008). Earthquake ground motion prediction using the ambient seismic field, *Geophys. Res. Lett.* **35,** L14304, doi: 10.1029/2008GL034428.

Prieto, G. A., M. Denolle, J. F. Lawrence, and G. C. Beroza (2011). On amplitude information carried by the ambient seismic field, *Compt. Rendus Geosci.* **343,** 600–614, doi: 10.1016/j.crte.2011.03.006.

Roten, D., K. B. Olsen, S. M. Day, Y. Cui, and D. Fäh (2014). Expected seismic shaking in Los Angeles reduced by San Andreas fault zone plasticity, *Geophys. Res. Lett.* **41,** 2769–2777, doi: 10.1002/2014GL059411.

Roux, P., K. G. Sabra, P. Gerstoft, W. A. Kuperman, and M. C. Fehler (2005). P-waves from cross-correlation of seismic noise, *Geophys. Res. Lett.* **32,** L19303, doi: 10.1029/2005GL023803.

Sabra, K. G., P. Gerstoft, P. Roux, W. A. Kuperman, and M. C. Fehler (2005). Extracting time-domain Green's function estimates from ambient seismic noise, *Geophys. Res. Lett.* **32,** L03310, doi: 10.1029/2004GL021862.

Shapiro, N. M., and M. Campillo (2004). Emergence of broadband Rayleigh waves from correlations of the ambient seismic noise, *Geophys. Res. Lett.* **31,** L07614, doi: 10.1029/2004GL019491.

Shapiro, N. M., M. Campillo, L. Stehly, and M. H. Ritzwoller (2005). High-resolution surface-wave tomography from ambient seismic noise, *Science* **307,** 1615–1618, doi: 10.1126/science.1108339.

Shapiro, N. M., M. H. Ritzwoller, and G. D. Bensen (2006). Source location of the 26 sec microseism from cross-correlations of ambient seismic noise, *Geophys. Res. Lett.* **33,** L18310, doi: 10.1029/2006GL027010.

Sheng, Y., M. A. Denolle, and G. C. Beroza (2017). Multicomponent C3 Green's functions for improved long-period ground-motion prediction, *Bull. Seismol. Soc. Am.* **107,** 2836, doi: 10.1785/0120170053.

Shiomi, K. (2013). New measurements of sensor orientation at NIED Hi-net stations, *Rep. NIED* **80,** 1–20.

Snieder, R. (2004). Extracting the Green's function from the correlation of coda waves: A derivation based on stationary phase, *Phys. Rev. E* **69,** 046610, doi: 10.1103/PhysRevE.69.046610.

Somerville, P., K. Irikura, R. Graves, S. Sawada, D. Wald, N. Abrahamson, Y. Iwasaki, T. Kagawa, N. Smith, and A. Kowada (1999). Characterizing crustal earthquake slip models for the prediction of strong ground motion, *Seismol. Res. Lett.* **70,** 59–80, doi: 10.1785/gssrl.70.1.59.

Stehly, L., and P. Boué (2017). On the interpretation of the amplitude decay of noise correlations computed along a line of receivers, *Geophys. J. Int.* **209,** 358, doi: 10.1093/gji/ggx021.

Stutzmann, E., J.-P. Montagner, A. Sebai, W. C. Crawford, J.-L. Thirot, P. Tarits, D. Stakes, B. Romanowicz, J.-F. Karczewski, J.-C. Koenig, *et al.* (2001). Moise: A prototype multiparameter ocean-bottom station, *Bull. Seismol. Soc. Am.* **91,** 885, doi: 10.1785/0120000035.

Suzuki, W., T. Iwata, K. Asano, and N. Yamada (2005). Estimation of the source model for the foreshock of the 2004 off the Kii peninsula earthquakes and strong ground motion simulation of the hypothetical Tonankai earthquake using the empirical Green's function method, *Earth Planets Space* **57,** 345–350, doi: 10.1186/BF03352574.

Takagi, R., K. Nishida, T. Maeda, and K. Obara (2018). Ambient seismic noise wavefield in Japan characterized by polarization analysis of Hi-net records, *Geophys. J. Int.* **215,** 1682–1699, doi: 10.1093/gji/ggy334.

The Headquarters for Earthquake Research Promotion (2013). *Long-Term Evaluation of Nankai Trough Earthquake Activity*, Second Ed., available at https://www.jishin.go.jp/main/chousa/13may_nankai/index.htm (last accessed May 2018) (in Japanese).

Tsai, V. C. (2011). Understanding the amplitudes of noise correlation measurements, *J. Geophys. Res.* **116,** no. B09311, doi: 10.1029/2011JB008483.

Viens, L., M. Denolle, H. Miyake, S. Sakai, and S. Nakagawa (2017). Retrieving impulse response function amplitudes from the ambient seismic field, *Geophys. J. Int.* **210,** 210–222, doi: 10.1093/gji/ggx155.

Viens, L., K. Koketsu, H. Miyake, S. Sakai, and S. Nakagawa (2016). Basin-scale Green's functions from the ambient seismic field recorded by MeSO-net stations, *J. Geophys. Res.* **121,** 2507–2520, doi: 10.1002/2016JB012796.

Viens, L., A. Laurendeau, L. F. Bonilla, and N. M. Shapiro (2014). Broadband acceleration time histories synthesis by coupling low-frequency ambient seismic field and high-frequency stochastic modelling, *Geophys. J. Int.* **199,** 1784–1797, doi: 10.1093/gji/ggu362.

Viens, L., H. Miyake, and K. Koketsu (2015). Long-period ground motion simulation of a subduction earthquake using the offshore-onshore ambient seismic field, *Geophys. Res. Lett.* **42,** 5282–5289, doi: 10.1002/2015GL064265.

Viens, L., H. Miyake, and K. Koketsu (2016). Simulations of long-period ground motions from a large earthquake using finite rupture modeling and the ambient seismic field, *J. Geophys. Res.* **121,** 2507–2520, doi: 10.1002/2016JB012796.

Watanabe, S., Y. Bock, D. Melgar, and K. Tadokoro (2018). Tsunami scenarios based on interseismic models along the Nankai trough, Japan, from seafloor and onshore geodesy, *J. Geophys. Res.* **123,** 2448–2461, doi: 10.1002/2017JB014799.

Weaver, R. L. (2011). On the amplitudes of correlations and the inference of attenuations, specific intensities and site factors from ambient noise, *Compt. Rendus Geosci.* **343,** 615–622, doi: 10.1016/j.crte.2011.07.001.

Webb, S. C., and W. C. Crawford (2010). Shallow-water broadband OBS seismology, *Bull. Seismol. Soc. Am.* **100,** 1770, doi: 10.1785/0120090203.

Yagi, Y. (2004). On the earthquakes that occurred southeast off Kii peninsula on September 5, 2004, available at https://www.kenken.go.jp/japanese/information/information/press/20040908.pdf (last accessed May 2019) (in Japanese).

Yoshimura, C., Y. Yamamoto, and Y. Hisada (2008). Long-period ground motion simulation of 2004 off the Kii peninsula earthquakes and prediction of future M8 class earthquakes along Nankai trough subduction zone, south of Japan Island, *Proc. of the 14th World Conf. on Earthq. Eng.*, Beijing, China, 12–17 October 2008.

Youngs, R., S.-J. Chiou, W. Silva, and J. Humphrey (1997). Strong ground motion attenuation relationships for subduction zone earthquakes, *Seismol. Res. Lett.* **68,** 58, doi: 10.1785/gssrl.68.1.58.

Zeng, X., and S. Ni (2010). A persistent localized microseismic source near the Kyushu Island, Japan, *Geophys. Res. Lett.* **37,** L24307, doi: 10.1029/2010GL045774.

Zhao, J. X., J. Zhang, A. Asano, Y. Ohno, T. Oouchi, T. Takahashi, H. Ogawa, K. Irikura, H. K. Thio, P. G. Somerville, *et al.* (2006). Attenuation relations of strong ground motion in Japan using site classification based on predominant period, *Bull. Seismol. Soc. Am.* **96,** 898, doi: 10.1785/0120050122.

Department of Earth and Planetary Sciences
Harvard University
20 Oxford Street
Cambridge, Massachusetts 02138 U.S.A.
viens.loic.58r@st.kyoto-u.ac.jp

Manuscript received 2 December 2018;
Published Online 18 June 2019